“Structural and Multidisciplinary Optimization” manuscript No.
(will be inserted by the editor)

Blood flow topology optimization considering a thrombosis model

Diego Hayashi Alonso [1] · **Emílio Carlos Nelli Silva** [1]

Received: date / Accepted: date

Abstract In the field of topology optimization for fluid flow design, there is a specific class of formulations directed to non-Newtonian fluids. One prominent case is when the fluid is blood. In this case, in addition to the non-Newtonian effect, the damage caused by the flow to the blood (i.e., blood damage) should be taken into account. Blood damage is essentially given by two types: hemolysis, which corresponds to the breakdown of Red Blood Cells (RBCs), and thrombosis, which corresponds to the formation of blood clotting. More specifically, in terms of thrombosis, blood clotting is formed by the aggregation of platelets and RBCs in vessels. Furthermore, in order to model thrombosis, there are essentially two approaches – *platelet activation* (initiation of thrombosis) and *platelet aggregation*. However, the computational cost of the second approach is still considered impractical for real applications. In the topology optimization field, hemolysis and thrombosis have been normally assumed to be indirectly minimized by considering the shear stress (or even energy dissipation or vorticity). However, a recent work has considered the direct minimization of hemolysis from a differential equation model. In terms of thrombosis, the stress levels for damage are 10 times lower than hemolysis, which means that it may not be sufficient to consider only the minimization of hemolysis in the design. Therefore, in this work, the topology optimization is formulated in order to take thrombosis into account, computed by a platelet activation model. The resulting formulation is also set to consider hemolysis and relative energy dissipation (as a way to indirectly maximize efficiency). In terms of thrombosis, the *shear-induced platelet activation* model is here rewritten for a finite elements approach, while also considering the necessary adjustments for the topology optimization formulation. The topology optimization is also formulated for a non-Newtonian fluid model for blood, and the optimization solver is IPOPT (Interior Point Optimization algorithm). Some numerical examples are presented considering 2D swirl flow configurations and a 2D configuration.

Keywords Fluid topology optimization · Thrombosis model · Hemolysis model · Blood flow · Finite element method · Automatic differentiation

1 Introduction

When designing blood flow devices, one important aspect is the minimization of blood damage, which is essentially given by hemolysis and thrombosis. The first mentioned blood damage source (hemolysis) is related to the breakdown of RBC membranes, which releases the RBC hemoglobin content into the plasma, and whose excessive occurrence may lead to renal failure (Garon and Farinas, 2004). Among the causes of hemolysis, there are the advent of high shear stresses and the exposure times of the RBCs to these stress levels, since the amount of damage caused to the RBCs depends on the exposure time to the higher shear stress levels (Behbahani et al., 2009; Ghattas et al., 1995; Garon and Farinas, 2004). Other effects, which are

---

Diego Hayashi Alonso
E-mail: diego.alonso@usp.br
ORCID: https://orcid.org/0000-0002-6032-9989

Emílio Carlos Nelli Silva
E-mail: ecnsilva@usp.br
ORCID: http://orcid.org/0000-0003-1715-1713

[1] Department of Mechatronics and Mechanical Systems Engineering, Polytechnic School of the University of São Paulo, SP, Brazil

Published article (Published: June 8th, 2022):
Alonso, D.H. & Silva, E.C.N. **Blood flow topology optimization considering a thrombosis model.** Struct Multidisc Optim 65, 179 (2022).
https://doi.org/10.1007/s00158-022-03251-8

normally neglected, are chemical, osmosis and thermal effects (Apel et al., 2001).

The second mentioned blood damage source (thrombosis) is the formation of blood clotting (thrombus), by aggregating platelets and RBCs in vessels (Packham, 1994), and is normally initiated by the body to prevent bleeding, but may be caused by abnormal conditions in the blood circulation, obstructing healthy vessels. The three main factors that lead to clotting are alterations in the blood flow, abnormalities of the vascular wall, and alterations in the constitution of blood (Behbahani et al., 2009; Bagot and Arya, 2008). This way, thrombosis can be caused by high shear stresses, stagnation/recirculation, and the contact of blood with surfaces with low hemocompatibility (Behbahani et al., 2009; Ding et al., 2015). If blood clotting is formed on the surface of a VAD (Ventricular Assist Device), it can compromise the function of the device. Furthermore, if the thrombus dettaches itself from the surface it was formed on, it may negatively affect the blood vessels of the whole body. According to Behbahani et al. (2009), thrombosis is one of the primary causes of death for patients with VADs.

The mechanism of thrombosis is directly related to platelet activation and aggregation. In fact, in VADs, platelets activate and aggregate (forming blood clotting – i.e., thrombus) due to mechanically induced high shear stress levels (Sheriff et al., 2013), requiring patients to take anti-coagulation medications, which may also lead to bleeding (Fraser et al., 2010). Platelet activation is closely related to the initiation of the formation of blood clotting thrombus (Yun et al., 2016). Since minimizing the platelet activation minimizes the risk of thrombosis and lowers the dose of anti-coagulation medications (Fraser et al., 2010), it is an important aspect that should be taken into account in the design of blood flow devices. In high speed VADs, the shear stresses acting in VADs can reach up to 800 Pa and extremely high shear stresses may act for short time intervals in the order of ms (Soares et al., 2013; Kini et al., 2001; Cheng et al., 2004). These brief durations of high shear stress levels may be sufficient to activate platelets and/or sensitize them (Sheriff et al., 2010). According to Soares et al. (2013), this sensitization means that the previously stressed platelets should not return to their pre-exposure condition, and should activate at higher shear stresses (Sheriff et al., 2010; Soares et al., 2013). According to Soares et al. (2013), the entire shear stress history must be taken into account to capture this effect. Another factor contributing to thrombosis is platelet aggregation (Chopard et al., 2017). However, according to Fraser et al. (2010), the models for platelet aggregation are complex and computationally high demanding, being therefore unsuitable for evaluating platelet aggregation in real fluid devices. It can also be highlighted that this means that the currently available platelet aggregation models are also unsuitable for topology optimization, since this computation would need to be repeated at each optimization iteration. Therefore, only platelet activation is considered in this work for evaluating thrombosis. In order to measure the level of platelet activation, the Platelet Activation State (PAS) index is normally used. The PAS index quantifies the contribution of platelet activation to the generation of thrombin, which is the protein responsible for activating platelets (Brass, 2003; Monroe et al., 2002; Consolo et al., 2016).

Some numerical prediction models for platelet activation are based on the same formulation used for the numerical prediction of the hemolysis index (Fraser et al., 2010). For example, the Giersiepen-Wurzinger correlation (basic correlation used for deriving the hemolysis models) can be used by changing the coefficients (Giersiepen et al., 1990; Sheriff et al., 2013). Some models that can be converted from hemolysis models to platelet activation models are: *linear damage index* (Giersiepen et al., 1990; Sheriff et al., 2013), *asymptotically consistent damage index* (Giersiepen et al., 1990; Sheriff et al., 2013), *mechanical dose infinitesimal damage index* (Hellums, 1994; Nobili et al., 2008), *infinitesimal damage index* (Sheriff et al., 2013), and *power law damage accumulation* (Alemu and Bluestein, 2007; Sheriff et al., 2013). In this work, the considered formulation is the *shear-induced platelet activation* model (Soares et al., 2013), which is not a reuse of a hemolysis model with different coefficients. It is able not only to capture the effect of the shear stress, but to capture the sensitization effect of the platelets, in which the necessary shear stress levels for the platelets to activate increases if the platelets are exposed to high shear stress levels for a certain time interval. However, the original formulation of this model is highly non-linear, which leads to numerical convergence issues when solving with the finite element method (Eulerian approach). For solving this problem, the original model is rewritten based on the mechanical dose definition by Hellums (1994), reducing the non-linearity of the model (*mechanical dose shear-induced PAS* model). Furthermore, an additional penalization term is included in this model for topology optimization.

When considering optimization, some blood flow devices that have to deal with blood damage during their operation are blood pumps (which may be part of VADs) and bypass grafts. In particular, the mechanical interaction of the blood flow with the device gives rise to the necessary stress conditions for blood damage (Garon and Farinas, 2004). It can also be noted that modern atraumatic designs are said to be able to avoid RBC breakdown (Behbahani et al., 2009). Yet, even when the damage is sublethal, the RBC damage should still be reduced, especially when considering middle to long operations of the blood flow devices, because the hemoglobin level of blood can rise even under minor blood damage, and may deteriorate the patient's condition, possibly leading to the failure of multiple organs and dysfunction of the kidneys (Behbahani et al., 2009).

Among the existing optimization methods, the most generic is the topology optimization method, which may distribute solid/fluid over the design domain and achieve any kind of formats and inclusions. Historically, it was first considered for fluid flow problems by Borrvall and Petersson (2003) through the *pseudo-density approach*. Various more complex fluid flow modeling have been considered throughout the years, about which an overview may be seen in Alexandersen and Andreasen (2020). One important aspect that requires specific considerations and adjustments to the topology optimization formulation is the non-Newtonian effect. The non-Newtonian effect is present in blood flow mainly by the shear-thinning effect (Gijsen et al., 1999), which is time-independent and is given, in this work, by the Carreau-Yasuda model (Gijsen et al., 1999; Pratumwal et al., 2017; Leondes, 2000). In terms of topology optimization for non-Newtonian fluids, some designs that have been previously performed are: roller-type blood viscous micropumps (Zhang et al., 2016), centrifugal bladed blood pumps (Romero and Silva, 2017), arterial bypass grafts (Zhang and Liu, 2015; Hyun et al., 2014; Kian, 2017), aneurism implants (Jiang et al., 2017), Tesla-type blood pumps (Alonso and Silva, 2021), and viscoelastic rectifier design (Jensen, 2013).

Antaki et al. (1995) were the first to consider the optimization of blood pumps with Computational Fluid Dynamics (CFD). The aspects that were considered are: minimizing the shear stress as an indirect minimization of hemolysis (Behbahani et al., 2009); minimizing the energy dissipation as a mean to improve the efficiency; and minimizing the vorticity so as to reduce the flow recirculation. For hemolysis, in centrifugal bladed blood pump topology optimization, Romero and Silva (2017) consider a simplified version of the hemolysis index which is closer to the real hemolysis index (Montevecchi et al., 1995). The real hemolysis index, based on the solution of a differential equation from a hemolysis model, was previously considered in Alonso and Silva (2021), from the *asymptotically consistent damage index* model (Farinas et al., 2006). Although hemolysis has been previously considered in optimization in general and, more recently, in topology optimization, thrombosis has been hardly considered in any type of optimization. This is attributed to the previous historical absence of validated models for thrombosis (Soares et al., 2013). However, it can be highlighted that thrombosis corresponds to stress levels that are 10 times lower than hemolysis (Sheriff et al., 2013; Travis et al., 2001; Soares et al., 2013), which means that, for reducing blood damage (hemolysis and thrombosis), it may not be sufficient to consider only the minimization of hemolysis. The minimization of thrombosis has already been considered indirectly by minimizing the vorticity (Romero and Silva, 2017) (or even the energy dissipation). However, so far, no previous work on topology optimization has considered the inclusion of a real measure of thrombosis, which is based on the solution of a set of differential equations (a thrombosis model), in the topology optimization formulation.

Therefore, the main objective of this work is to include a thrombosis model (*mechanical dose shear-induced PAS* model) in the blood flow (non-Newtonian) topology optimization formulation. Furthermore, a hemolysis model, which is selected as the *asymptotically consistent damage index* model (Farinas et al., 2006; Alonso and Silva, 2021), is also included in the formulation. Therefore, the objective functions considered in the optimization are given as: minimizing the relative energy dissipation from the viscous, porous and inertial effects (Borrvall and Petersson, 2003; Alonso et al., 2019); and minimizing blood damage, from the hemolysis and thrombosis values, both computed from hemolysis and thrombosis models, respectively. Some of the numerical examples consider the use of the *2D swirl flow model*. The use of a 2D swirl flow model simplifies the complete 3D fluid flow model (more computationally expensive), by considering a 2D axisymmetric mesh. It can be considered when there is an axisymmetric flow with a rotation around an axis (swirl flow), being able to model, for example, bladeless blood pump devices (*Tesla blood pumps*). The modeling of the fluid flow is solved from the finite element method, while the material model is given as the traditional version of Borrvall and Petersson (2003) augmented by an additional inertial effect (Philippi and Jin, 2015; Alonso and Silva, 2021). The design variable is assumed as nodal. An additional penalization scheme is also considered for the non-Newtonian viscosity (Hyun et al., 2014; Alonso et al., 2020), enforcing a low shear stress behavior for blood within the modeled solid material. The finite element method is implemented in the FEniCS platform, the sensitivities are computed from the adjoint method (Farrell et al., 2013; Mitusch et al., 2019), the optimizer is the interior point algorithm IPOPT (Wächter and Biegler, 2006), and MUMPS (Amestoy et al., 2001) is the solver of the weak form of the problem, for the equations that are linearized for the Newton-Raphson method of the simulation.

This paper is organized as follows: in Section 2, the derivation of the fluid flow models is briefly performed, alongside the definition of the non-Newtonian fluid model; in Section 3, the thrombosis and hemolysis models are described; in Section 4, the topology optimization is written for the blood damage models (hemolysis and thrombosis), and the Brinkman-Forchheimer model; in Section 5, the numerical implementation is described; in Section 6, some numerical results are presented; and in Section 7, some conclusions are inferred.

2 Fluid flow equilibrium equations

The continuity equation and the linear momentum (Navier-Stokes) equation are used to model the fluid flow, whilst considering incompressible non-Newtonian fluid at a steady-state flow regime and a rotational reference frame. The formulation also includes a porosity model and is mainly presented for the case of considering the 2D swirl flow model, but the necessary changes for considering a 2D model are also mentioned (Munson et al., 2009; White, 2009; Romero and Silva, 2014)

$$\nabla \bullet \boldsymbol{v} = 0 \tag{1}$$

$$\rho \nabla \boldsymbol{v} \bullet \boldsymbol{v} = \nabla \bullet \boldsymbol{T} + \rho \boldsymbol{f} - 2\rho(\boldsymbol{\omega} \wedge \boldsymbol{v}) - \rho \boldsymbol{\omega} \wedge (\boldsymbol{\omega} \wedge \boldsymbol{r}) + \boldsymbol{f}_r(\alpha) \tag{2}$$

where $\boldsymbol{v}$ and p are the relative velocity (in relation to the rotating reference frame) and the pressure, respectively. The fluid properties are given by ρ (density of the fluid), and $\mu(\dot{\gamma}_{\mathrm{m}})$ (viscosity of the non-Newtonian fluid). A body force acting on the fluid per unit volume $\rho \boldsymbol{f}$ is also included for completeness. The inertial forces from the rotating reference frame are $-2\rho(\boldsymbol{\omega} \wedge \boldsymbol{v})$ and $-\rho \boldsymbol{\omega} \wedge (\boldsymbol{\omega} \wedge \boldsymbol{r})$, where $\wedge$ denotes cross product. The radial position in the fluid with respect to the rotation axis is given by $\boldsymbol{r}$ (in 2D swirl flow, it is equivalent to use $\boldsymbol{s}$, which is the position of the fluid). The resistance force of the porous medium, which is the additional force term considered in topology optimization for modeling the solid material, is given by $\boldsymbol{f}_r(\alpha)$, where α is the pseudo-density (i.e., the design variable in topology optimization), with values in the interval between 0 (solid) and 1 (fluid), and $\boldsymbol{T}$ is the fluid stress tensor, which is defined by

$$\boldsymbol{T} = 2\mu(\dot{\gamma}_{\mathrm{m}})\boldsymbol{\epsilon} - p\boldsymbol{I} \ , \ \boldsymbol{\epsilon} = \frac{1}{2}(\nabla \boldsymbol{v} + \nabla \boldsymbol{v}^T) \tag{3}$$

When considering the 2D swirl flow model, the definitions of the differential operators are changed to their cylindrical coordinates counterparts (with respect to the usual Cartesian coordinates differential operators). The axisymmetry assumption of the 2D swirl flow model means that $\frac{\partial v_r}{\partial \theta} = \frac{\partial v_\theta}{\partial \theta} = \frac{\partial v_z}{\partial \theta} = \frac{\partial p}{\partial \theta} = 0$, leading to:

$$\boldsymbol{s} = (r,\ 0,\ z) = r\boldsymbol{e}_r + z\boldsymbol{e}_z \tag{4}$$

$$\boldsymbol{v} = (v_r,\ v_\theta,\ v_z) = v_r\boldsymbol{e}_r + v_\theta\boldsymbol{e}_\theta + v_z\boldsymbol{e}_z \tag{5}$$

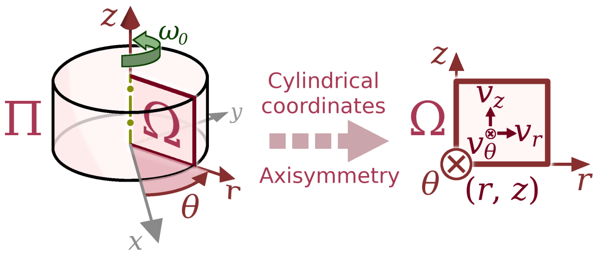

Fig. 1: Illustration of the 2D swirl flow model.

The resulting finite element formulation is further detailed in Appendix A.

2.1 Non-Newtonian fluid model

The non-Newtonian behavior of blood is mainly led by the shear-thinning effect (Gijsen et al., 1999), which is time-independent. The shear-thinning effect may be considered through the Carreau-Yasuda model (Gijsen et al., 1999; Pratumwal et al., 2017; Leondes, 2000), which is given by (Cho and Kenssey, 1991; Bird et al., 1987)

$$\mu(\dot{\gamma}_{\mathrm{m}}) = \mu_\infty + (\mu_0 - \mu_\infty)[1 + (\lambda\dot{\gamma}_{\mathrm{m}})^a]^{\frac{n-1}{a}} \tag{6}$$

where a is the Yasuda coefficient, n is an exponential factor, λ is a time constant (*characteristic time*), μ_0 is the maximum (*low-shear stress*) dynamic viscosity and μ_∞ is the minimum (*high-shear stress*) dynamic viscosity. It is possible to compute the shear rate magnitude (*scalar shear rate*) $\dot{\gamma}_{\mathrm{m}}$ as (Lai et al., 2009)

$$\dot{\gamma}_{\mathrm{m}} = \sqrt{2\boldsymbol{\epsilon} \bullet \boldsymbol{\epsilon}} \tag{7}$$

where $\boldsymbol{\epsilon}$ is the viscous stress deformation tensor $\boldsymbol{\epsilon} = \frac{1}{2}(\nabla \boldsymbol{v} + \nabla \boldsymbol{v}^T)$, and " $\bullet$ " is the inner product, as defined in Gurtin (1981).

3 Blood damage modeling

As a requirement for computing the blood damage, it is necessary to compute the shear stress magnitude (also referred to as *scalar shear stress*), which acts on the blood, having an important role in blood damage. For this computation, there are two main approaches (Arora et al., 2004, 2012): stress-based (based on the shear stress computed in the fluid) and strain-based (based on RBC distortion and viscoelastic deformation).

Since the strain-based approach requires the computation of a tensorial equation (Arora et al., 2004, 2012; Barthes-Biesel and Rallison, 1981), which may pose a high computational cost, the stress-based approach is considered in this work. The stress-based approach considers immediate deformation of the RBCs – which is unrealistic when considering physiological conditions (Pauli et al., 2013) – and does not take the residence time (i.e., the interval of time in which the RBCs are inside the device, affecting the RBC shape distortion) into account, which is normally small for blood pumps (Pauli et al., 2013). These assumptions mean that the stress-based approach should lead to an overprediction of the blood damage (Pauli et al., 2013). In the stress-based approach, the shear stress magnitude can be given as (Tesch, 2013; Arora et al., 2004, 2012; Alemu and Bluestein, 2007; Wu et al., 2005)

$$\tau_\mathrm{m} = \sqrt{2\boldsymbol{\tau}\bullet\boldsymbol{\tau}},\ \boldsymbol{\tau} = \mu(\dot{\gamma}_\mathrm{m})(\nabla \boldsymbol{v} + \nabla \boldsymbol{v}^T) \tag{8}$$

The equations in this Section are presented according to the 2D swirl flow model, but they can be converted to the 2D model by omitting the "$2\pi r$" (or "r") factor in the equations.

The local thrombosis and hemolysis values, which are I_{PAS} (local PAS index) and I_H (local hemolysis index), respectively, are considered with 1^{st} degree interpolation (P_1 element) in the finite element modeling.

3.1 Thrombosis modeling

For numerically modeling the PAS index, a local definition of this index is required, which is given by

$$I_{PAS} = \frac{r_\mathrm{tg}}{r_\mathrm{tg,full}} \tag{9}$$

where I_{PAS} is the local PAS index, r_tg is the rate of thrombin generation of the activated platelets and $r_\mathrm{tg,full}$ is the rate of thrombin generation of fully activated platelets (i.e., the maximum thrombin generation capacity).

Then, the PAS index $I_{PAS,T}$, which is here referred to as the total PAS index, may be expressed as

$$\begin{aligned} I_{PAS,T} =& \frac{\Delta r_\mathrm{tg}}{r_\mathrm{tg,full}} = \frac{r_\mathrm{tg,out} - r_\mathrm{tg,in}}{r_\mathrm{tg,full}} = \frac{r_\mathrm{tg,out}}{r_\mathrm{tg,full}} - \frac{r_\mathrm{tg,in}}{r_\mathrm{tg,full}} \\ =& \frac{\int_{\Gamma_{\Omega,\mathrm{out}}} I_{PAS}(\boldsymbol{v}\bullet\boldsymbol{n})2\pi r d\Gamma_\mathrm{out}}{\int_{\Gamma_{\Omega,\mathrm{out}}}(\boldsymbol{v}\bullet\boldsymbol{n})2\pi r d\Gamma_\mathrm{out}} \\ &- \frac{\int_{\Gamma_{\Omega,\mathrm{in}}} I_{PAS}(\boldsymbol{v}\bullet\boldsymbol{n})2\pi r d\Gamma_\mathrm{in}}{\int_{\Gamma_{\Omega,\mathrm{in}}}(\boldsymbol{v}\bullet\boldsymbol{n})2\pi r d\Gamma_\mathrm{in}} \\ =& \frac{\oint_\Gamma I_{PAS}(\boldsymbol{v}\bullet\boldsymbol{n})d\Gamma}{Q} \end{aligned} \tag{10}$$

where $\Delta r_\mathrm{tg} = r_\mathrm{tg,out} - r_\mathrm{tg,in}$ is the variation of the rate of thrombin generation of the activated platelets, and Q is the flow rate, which may be given from the outflow or from the inflow:

$$Q = \int_{\Gamma_\mathrm{out}} (\boldsymbol{v}\bullet\boldsymbol{n})2\pi r d\Gamma_\mathrm{out} = -\int_{\Gamma_\mathrm{in}} (\boldsymbol{v}\bullet\boldsymbol{n})2\pi r d\Gamma_\mathrm{in} \tag{11}$$

The *mechanical dose shear-induced PAS* model is a *mechanical dose*-based version of the *shear-induced platelet activation* model (Soares et al., 2013). As in the original *shear-induced platelet activation* model (Soares et al., 2013), this model is based on three effects (sensitization, stress level and stress rate), and also on a correction for platelets that are not activated. An additional term is included herein to penalize the PAS index inside the modeled solid material. The terms are described as follows:

1. **Sensitization effect**: The sensitization effect depends on the current level of activation (PAS index, I_{PAS}) and explicitly on the total shear stress accumulation of the entire history up to time "t" ($\int_0^t \tau_\mathrm{m} dt$). The form of this term has been experimentally determined (Soares et al., 2013) based on experimental data from Sheriff et al. (2010), which shows that platelets that were exposed to high shear stresses showed significantly higher rates of activation than platelets that were not exposed to these high shear stresses (Sheriff et al., 2010, 2013). It may be given for each pathline from:

$$S_\tau = \int_0^t \tau_\mathrm{m} dt \tag{12}$$

$$\Delta I_{PAS,S} = C_{PAS,S} I_{PAS} S_\tau \Delta t \tag{13}$$

where $I_{PAS,S}$ is the PAS index contribution from the sensitization effect, S_τ is the *shear stress history*, and $C_{PAS,S}$ is the proportionality factor for the sensitization effect.

The corresponding differential forms become:

$$\frac{DS_\tau}{Dt} = \tau_\mathrm{m} \tag{14}$$

$$\frac{DI_{PAS,S}}{Dt} = C_{PAS,S} I_{PAS} S_\tau \tag{15}$$

2. **Stress level effect**: The stress level effect is based on the Giersiepen-Wurzinger correlation (Giersiepen et al., 1990). For the case of platelet activation, the Giersiepen-Wurzinger correlation adapted for each pathline becomes:

$$\Delta I_{PAS,sl} = C_{PAS,sl} \tau_\mathrm{m}^{\alpha_s} \Delta t^{\alpha_t} \tag{16}$$

where $I_{PAS,sl}$ is the PAS index contribution from the shear level effect, α_s is the shear stress level exponent, and α_t is the stress level exposure time exponent.

The original formulation of the *shear-induced platelet activation* model (Soares et al., 2013) assumes an infinitesimal time step ($\Delta t \to 0^+$), τ_m being time-independent in eq. (16), and considers the power rule for derivatives, $\frac{D(I_{PAS}^{\frac{1}{\alpha_t}})}{Dt} = \frac{1}{\alpha_t} {I_{PAS}}^{\frac{1}{\alpha_t}-1} \frac{DI_{PAS}}{Dt}$. Therefore,

$$\frac{DI_{PAS,sl}}{Dt} = C_{PAS,sl}^{\frac{1}{\alpha_t}} \alpha_t \tau_\mathrm{m}^{\frac{\alpha_s}{\alpha_t}} {I_{PAS}}^{\frac{\alpha_t-1}{\alpha_t}} \tag{17}$$

As can be noticed, there is a clear non-linearity present in eq. (17) due to the exponent of I_{PAS}. To avoid it, the mechanical dose approach (Hellums, 1994; Nobili et al., 2008) is considered, which, particularly, makes convergence more difficult. The mechanical dose approach is an approach that rewrites the blood damage equations, and has already been considered in the formulation of one of the existing hemolysis models – i.e., the *mechanical dose infinitesimal damage index* model (Grigioni et al., 2005). In the mechanical dose approach, a *mechanical dose of PAS from the stress level* is defined as $\Delta D_{PAS,sl} = \tau_\mathrm{m}^{\frac{\alpha_s}{\alpha_t}} \Delta t$, which, from eq. (16), leads to

$$\Delta I_{PAS,sl} = C_{PAS,sl} \Delta D_{PAS,sl}^{\alpha_t} \tag{18}$$

By assuming an infinitesimal time step ($\Delta t \to 0^+$) and τ_m being time-independent, the differential forms from eq. (18) become:

$$\frac{DD_{PAS,sl}}{Dt} = \tau_\mathrm{m}^{\frac{\alpha_s}{\alpha_t}} \tag{19}$$

$$\frac{DI_{PAS,sl}}{Dt} = C_{PAS,sl} \alpha_t D_{PAS,sl}^{\alpha_t - 1} \frac{DD_{PAS,sl}}{Dt} \tag{20}$$

3. **Stress rate effect**: The stress rate effect considers a formulation that is analogous to the Giersiepen-Wurzinger correlation. The resulting formulation was found by Soares et al. (2013) to correlate well to previous experimental data:

$$\Delta I_{PAS,sr} = C_{PAS,sr} |\dot{\tau}_\mathrm{m}|^{\delta_s} \Delta t^{\delta_t} \tag{21}$$

where $I_{PAS,sr}$ is the PAS index contribution from the shear rate effect, δ_s is the shear stress rate exponent, δ_t is the stress rate exposure time exponent, and $\dot{\tau}_\mathrm{m} = \frac{D\tau_\mathrm{m}}{Dt}$. As an observation, Hansen et al. (2015) considers $\dot{\tau}_\mathrm{m}$ to be small and, therefore, neglects it.

The original formulation of the *shear-induced platelet activation* model (Soares et al., 2013) assumes $\ddot{\tau}_\mathrm{m} = \frac{D^2\tau_\mathrm{m}}{Dt^2} = 0$, leading to

$$\frac{DI_{PAS,sr}}{Dt} = C_{PAS,sr}^{\frac{1}{\delta_t}} \delta_t \left| \frac{D\tau_\mathrm{m}}{Dt} \right|^{\frac{\delta_s}{\delta_t}} {I_{PAS}}^{\frac{\delta_t - 1}{\delta_t}} \tag{22}$$

From the exponent of I_{PAS} in eq. (22), which poses a clear non-linearity, and from the same reason presented for the stress level effect, the *mechanical dose of PAS from the stress rate* is defined as $\Delta D_{PAS,sr} = \tau_\mathrm{m}^{\frac{\delta_s}{\delta_t}} \Delta t$, which, from eq. (21), leads to

$$\Delta I_{PAS,sr} = C_{PAS,sr} \Delta D_{PAS,sr}^{\delta_t} \tag{23}$$

By assuming $\ddot{\tau}_\mathrm{m} = \frac{D^2\tau_\mathrm{m}}{Dt^2} = 0$, the differential forms from eq. (23) become:

$$\frac{DD_{PAS,sr}}{Dt} = \left| \frac{D\tau_\mathrm{m}}{Dt} \right|^{\frac{\delta_s}{\delta_t}} \tag{24}$$

$$\frac{DI_{PAS,sr}}{Dt} = C_{PAS,sr} \delta_t D_{PAS,sr}^{\delta_t - 1} \frac{DD_{PAS,sr}}{Dt} \tag{25}$$

4. **Correction term for non-activated platelets**: The original formulation of the *shear-induced platelet activation* model (Soares et al., 2013) also considers a *correction term for non-activated platelets*, which is analogous to the corresponding one in the *asymptotically consistent damage index* model (Farinas et al., 2006), and consists in multiplying all the effects by $(1 - I_{PAS})$. Soares et al. (2013) also suggests that other saturation terms, such as a sigmoidal function (Gompertz function), may be used instead of the linear correction $(1 - I_{PAS})$. When considering the mechanical dose approach (Hellums, 1994; Nobili et al., 2008), this correction is not required for bounding I_{PAS} between

0 and 1; however, this correction may be useful for the sensitization effect, which means that it is included in this work.

5. **Solid material penalization**: An additional term is included in the I_{PAS} equation – i.e., in eq.(30), which is presented ahead in this section. The additional term is used to penalize the PAS index inside the modeled solid material. This term is given as:

$$S_p = \kappa_{PAS}(\alpha)(I_{PAS} - I_{PAS,\mathrm{mat}}) \tag{26}$$

where $\kappa_{PAS}(\alpha)$ is an additional penalization parameter for the PAS index, and $I_{PAS,\mathrm{mat}}$ is the value of the PAS index being imposed inside the modeled solid material. $I_{PAS,\mathrm{mat}}$ can be set, for example, as $I_{PAS,\mathrm{mat}} = 10^{-14}$ (a small value). In eq. (26), when $\alpha = 1$ (i.e., there is fluid), $\kappa_{PAS}(\alpha)$ assumes its minimum value, which is normally zero, meaning that the rest of the equations are solved as if this additional term did not exist. When $\alpha = 0$ (i.e., there is solid), $\kappa_{PAS}(\alpha)$ assumes its maximum value, which is sufficiently high (user selected), and acts to enforce that $I_{PAS} = I_{PAS,\mathrm{mat}} \approx 0$. Therefore, the additional penalization term from eq. (26) only acts in topology optimization, aiming to achieve approximately zero local PAS index inside the modeled solid material. This is important, because, although the velocities inside the modeled solid material are extremely small, they may result in zones with high potential for thrombosis, which may, therefore, hinder the computation of the PAS index, and the topology optimization itself.

The complete differential form is obtained by combining the five presented effects (sensitization, stress level, stress rate, correction term for non-activated platelets, and solid material penalization). By also unfolding the material derivative terms in the relative reference frame, $\frac{D()}{Dt} = \frac{\partial()}{\partial t} + (\boldsymbol{v}\bullet\nabla)()$, and assuming steady state flow, the *mechanical dose shear-induced PAS* model in the differential form becomes a set of 3 linear differential equations and 1 non-linear differential equation:

$$(\boldsymbol{v}\bullet\nabla)S_\tau = \tau_\mathrm{m} \tag{27}$$

$$(\boldsymbol{v}\bullet\nabla)D_{PAS,sl} = \tau_\mathrm{m}^{\frac{\alpha_s}{\alpha_t}} \tag{28}$$

$$(\boldsymbol{v}\bullet\nabla)D_{PAS,sr} = |(\boldsymbol{v}\bullet\nabla)\tau_\mathrm{m}|^{\frac{\delta_s}{\delta_t}} \tag{29}$$

$$(\boldsymbol{v}\bullet\nabla)I_{PAS} = [S_e + S_\ell + S_r](1 - I_{PAS}) + S_p \tag{30}$$

where S_e represents the sensitization effect, S_ℓ represents the stress level effect, S_r represents the stress rate effect, $(1 - I_{PAS})$ is the correction term for non-activated platelets, and S_p is the solid material penalization. These terms are given as:

$$\begin{aligned}
S_e &= C_{PAS,S} I_{PAS} S_\tau \\
S_\ell &= C_{PAS,sl}\alpha_t D_{PAS,sl}^{\alpha_t - 1}(\boldsymbol{v}\bullet\nabla)D_{PAS,sl} \\
S_r &= C_{PAS,sr}\delta_t D_{PAS,sr}^{\delta_t - 1}(\boldsymbol{v}\bullet\nabla)D_{PAS,sr} \\
S_p &= \kappa_{PAS}(\alpha)(I_{PAS} - I_{PAS,\mathrm{mat}})
\end{aligned} \tag{31}$$

Eqs. (27), (28), (29) and (30) are then solved through an LSFEM (Least Squares Finite Element Method) approach (Nam et al., 2011; Pauli et al., 2013; Alonso and Silva, 2021). The resulting equations are shown in Appendix B.

Since no boundary terms appear in the equations of the LSFEM formulation (Appendix B), the only imposed boundary conditions are Dirichlet boundary conditions on the inlet, which may consist, for example, of zero inlet thrombosis ($S_\tau = 0$, $D_{PAS,sl} = 0$, $D_{PAS,sr} = 0$, $I_{PAS} = 0$).

Since eqs. (27), (28), (29) and (30) are independent, they may be solved independently and, therefore, sequentially.

Specifically for 2D swirl flow, eqs. (27), (28), (29) and (30) can be computed with velocities in the relative ($\boldsymbol{v}$) or absolute reference frames ($\boldsymbol{v}_\mathrm{abs} = \boldsymbol{v} + \boldsymbol{\omega}\wedge\boldsymbol{r}$). This is due to the axisymmetry assumption, which implies that the derivatives in relation to θ are zero. Thus, for 2D swirl flow, $(\boldsymbol{v}\bullet\nabla)a = (\boldsymbol{v}_\mathrm{abs}\bullet\nabla)a$, where "$a$" is a scalar (Lai et al., 2009). Note that other cases, such as 2D bladed pump (Romero and Silva, 2014), do not portray this correspondence, since an additional tangential acceleration effect (θ direction) appears, which would represent the movement of the computational domain (* In the 2D swirl flow case, the mesh does not change when under rotation).

3.2 Hemolysis modeling

Since the hemolysis model is also computed for comparison purposes, the corresponding model is reproduced in this section. The hemolysis index $I_{H,T}$, which is here referred to as the total hemolysis index, is given with respect to the local hemolysis index I_H as

$$\begin{aligned}
I_{H,T} &= \frac{\int_{\Gamma_\mathrm{out}} I_H(\boldsymbol{v}\bullet\boldsymbol{n})2\pi r d\Gamma_\mathrm{out}}{\int_{\Gamma_\mathrm{out}}(\boldsymbol{v}\bullet\boldsymbol{n})2\pi r d\Gamma_\mathrm{out}} - \frac{\int_{\Gamma_\mathrm{in}} I_H(\boldsymbol{v}\bullet\boldsymbol{n})2\pi r d\Gamma_\mathrm{in}}{\int_{\Gamma_\mathrm{in}}(\boldsymbol{v}\bullet\boldsymbol{n})2\pi r d\Gamma_\mathrm{in}} \\
&= \frac{\oint_\Gamma I_H(\boldsymbol{v}\bullet\boldsymbol{n})2\pi r d\Gamma}{Q}
\end{aligned} \tag{32}$$

The *asymptotically consistent damage index* model is considered to model hemolysis, and is solved by a LS-FEM formulation (Nam et al., 2011; Pauli et al., 2013; Alonso and Silva, 2021). The *asymptotically consistent damage index* model is given as:

$$(\boldsymbol{v}\bullet\nabla)I_{H,L} = C_H^{\frac{1}{\beta_t}} \tau_{\mathrm{m}}^{\frac{\beta_s}{\beta_t}} (1 - I_{H,L}) \tag{33}$$

The hemolysis model formulation, from eq. (33), does not require an additional penalization term, because it depends essentially on the value of the total shear stress magnitude, which does not induce high values within the modeled solid material. However, the PAS formulation, from eqs. (27), (28), (29) and (30), depends on the *shear stress history*, which may significantly increase the platelet activation that occurs inside the modeled solid material. This high value inside the solid material can hinder the topology optimization process and may be reduced by the additional penalization term.

4 Topology optimization problem formulation

4.1 Resistance force of the modeled solid material

The resistance force of the solid material modeled in this work is considered for the Brinkman-Forchheimer model, which consists of the Brinkman model (Borrvall and Petersson, 2003) including an additional inertial effect (Forchheimer, 1901; Philippi and Jin, 2015; Alonso and Silva, 2021). Both models – Brinkman (Borrvall and Petersson, 2003) and Brinkman-Forchheimer (Philippi and Jin, 2015; Alonso and Silva, 2021) – have already been previously considered in topology optimization. The Brinkman-Forchheimer model consists of the following expression for the resistance force of the modeled solid material (Alonso and Silva, 2021):

$$\boldsymbol{f}_r(\alpha) = \underbrace{-\kappa(\alpha)\boldsymbol{v}_{\mathrm{mat}}}_{\text{Darcy term}} \underbrace{-k_{\mathrm{inertia}}\sqrt{\kappa(\alpha)}|\boldsymbol{v}_{\mathrm{mat}}|\boldsymbol{v}_{\mathrm{mat}}}_{\text{Forchheimer term}} \tag{34}$$

where $\kappa(\alpha)$ is the inverse permeability, $k_{\mathrm{inertia}} = \frac{\rho}{\sqrt{\mu(\dot{\gamma}_{\mathrm{m}})}} C_F$ is the inertial resistance factor, $C_F = 0.55$ (Philippi and Jin, 2015; Ward, 1964), and $\boldsymbol{v}_{\mathrm{mat}}$ is the velocity in relation to the modeled solid material ($\boldsymbol{v}_{\mathrm{mat}} = (v_r,\ v_\theta - \omega_{\mathrm{mat}} r,\ v_z)$, where ω_{mat} is the rotation of the modeled solid material with respect to the reference frame).

Although the Brinkman-Forchheimer model is considered in this work, the Brinkman model (eq. (34) without the *Forchheimer term*) can also be considered, as long as the optimization parameters are readjusted to guarantee that the fluid flow is being sufficiently blocked and the topology optimization problem is well-conditioned (i.e., without excessively high topology optimization parameters).

4.2 Inverse permeability material model

For a well-conditioned topology optimization formulation, a relaxation (i.e., an interpolation) is considered between the solid ($\alpha = 0$) and fluid ($\alpha = 1$) materials (Borrvall and Petersson, 2003)

$$\kappa(\alpha) = \kappa_{\max} + (\kappa_{\min} - \kappa_{\max})\alpha\frac{1+q}{\alpha+q} \tag{35}$$

where the inverse permeability $\kappa(\alpha)$ is given between a maximum value ($\kappa_{\max}$) and a minimum value ($\kappa_{\min}$), with the penalization parameter $q > 0$ guiding its convexity, that is, when q assumes a large value, the material model becomes less relaxed.

4.3 Non-Newtonian viscosity material model (penalization)

The non-Newtonian viscosity, from eq. (6), is penalized inside the solid material as (Hyun et al., 2014; Alonso et al., 2020; Alonso and Silva, 2021)

$$\mu(\alpha, \dot{\gamma}_{\mathrm{m}}) = \mu_0 + (\mu(\dot{\gamma}_{\mathrm{m}}) - \mu_0)\alpha\frac{1+q}{\alpha+q} \tag{36}$$

where the fluid viscosity is interpolated between its *non-Newtonian* value, which is given by $\mu(\dot{\gamma}_{\mathrm{m}})$, from eq. (6), and its *low shear stress* value (μ_0). The penalization parameter (q) is set as the same considered in eq. (35). When considering eq. (36), $\mu(\dot{\gamma}_{\mathrm{m}})$ is replaced with $\mu(\alpha, \dot{\gamma}_{\mathrm{m}})$ in the equations of the previous sections.

4.4 PAS index material model

The material model for the solid material penalization of the PAS index is given as:

$$\kappa_{PAS}(\alpha) = \kappa_{PAS,\max} + (\kappa_{PAS,\min} - \kappa_{PAS,\max})\alpha\frac{1+q}{\alpha+q} \tag{37}$$

where $\kappa_{PAS,\max}$ and $\kappa_{PAS,\min}$ are, respectively, the maximum and minimum values of the additional penalization parameter $\kappa_{PAS}(\alpha)$. The penalization parameter (q) is the same as that of eq. (35). $\kappa_{PAS,\min}$ is set as zero, so that the modeled solid material includes the additional penalization.

4.5 Topology optimization problem

The formulation of the topology optimization problem is given as:

$$\boxed{\begin{array}{l}\mathbf{\min_{\alpha}}\ J(\boldsymbol{u}(\alpha),\alpha,I_{PAS}(\boldsymbol{u}(\alpha),\alpha),I_H(\boldsymbol{u}(\alpha),\alpha))\\ \textbf{such that}\\ \quad\text{Fluid volume constraint: } \displaystyle\int_{\Omega_\alpha}\alpha(2\pi r d\Omega_\alpha)\leqslant fV_0\\ \quad\text{Box constraint of } \alpha\text{: } 0\ \leqslant\ \alpha\leqslant\ 1\end{array}} \tag{38}$$

where $\boldsymbol{u}(\alpha) = \begin{bmatrix} p(\alpha) \\ \boldsymbol{v}(\alpha) \end{bmatrix}$ represents the state vector of the fluid flow simulation result (for a given distribution of α), f is the specified maximum fluid volume fraction, $V_0 = \int_{\Omega_\alpha} 2\pi r d\Omega_\alpha$ is the volume of the design domain (represented as Ω_α), $J(\boldsymbol{u}(\alpha),\alpha,I_{PAS}(\boldsymbol{u}(\alpha),\alpha),I_H(\boldsymbol{u}(\alpha),\alpha))$ is the multi-objective function, $I_{PAS}(\boldsymbol{u}(\alpha),\alpha)$ is computed from eqs. (27), (28), (29) and (30) sequentially, and $I_H(\boldsymbol{u}(\alpha),\alpha)$ is computed from eq. (33). Note that $2\pi r d\Omega_\alpha$ (2D swirl flow) is changed to $d\Omega_\alpha$ for 2D flow.

4.6 Multi-objective function

There are three objective functions considered herein, the relative energy dissipation (aiming to maximize the efficiency), the PAS index (aiming to minimize thrombosis), and the hemolysis index (aiming to minimize hemolysis):

The relative energy dissipation objective function is based on the definition presented in Borrvall and Petersson (2003), but also including the inertial effects for a rotating reference frame (Alonso et al., 2020). There is a close relationship between the computation of the relative energy dissipation and the pressure head in the fluid flow (Borrvall and Petersson, 2003). By also neglecting the presence of external body forces,

$$\begin{aligned}\Phi_{\text{rel}} = &\int_\Omega \left[\frac{1}{2}\mu(\dot{\gamma}_{\text{m}})(\nabla\boldsymbol{v}+\nabla\boldsymbol{v}^T)\bullet(\nabla\boldsymbol{v}+\nabla\boldsymbol{v}^T)\right]2\pi r d\Omega\\ &-\int_\Omega \boldsymbol{f}_r(\alpha)\bullet\boldsymbol{v}2\pi r d\Omega\\ &+\int_\Omega (2\rho(\boldsymbol{\omega}\wedge\boldsymbol{v})+\rho\boldsymbol{\omega}\wedge(\boldsymbol{\omega}\wedge\boldsymbol{r}))\bullet\boldsymbol{v}2\pi r d\Omega\end{aligned} \tag{39}$$

The total PAS index is computed by eq. (10), and is modeled by the *mechanical dose shear-induced PAS* model.

The total hemolysis index is computed from eq. (32), and is modeled from the *asymptotically consistent damage index* model.

The multi-objective function is defined for the three objective functions. To leverage the influence of each objective function in topology optimization, the multi-objective function is here considered in a logarithmic approach. Note that, when considering the logarithmic approach, the objective function becomes independent from the measurement unit. This can be viewed from the logarithm product rule, since ln([constant]f) = ln([constant]) + ln(f), meaning that the conversion between measurement units (represented by "[constant]") of an objective function "f" becomes a summed constant ("ln([constant])"), which does not influence the optimization procedure. There are three objective functions (Φ_{rel}, $I_{H,T}$ and $I_{PAS,T}$). Among these, $I_{H,T}$ and $I_{PAS,T}$ are strictly positive (i.e., $0 < I_{H,T} < 1$ and $0 < I_{PAS,T} < 1$). However, Φ_{rel} may be positive or negative, depending on whether the fluid flow device is pumping fluid or not. When the fluid flow device is not pumping fluid, such as in channels, no external energy is being supplied, and, therefore, Φ_{rel} is always positive. Fluid flow devices that pump fluid should always achieve negative Φ_{rel} values. In order to consider these two cases, two multi-objective functions are considered, being one for minimizing $\Phi_{\text{rel}} > 0$ and another one for minimizing $\Phi_{\text{rel}} < 0$. Then, the logarithmic multi-objective functions are given as:

1) For minimizing $\Phi_{\text{rel}} > 0$,

$$\begin{aligned}J = f_{\text{scal}}\Big[&w_\Phi \ln(\Phi_{\text{rel}})\\ &+w_{PAS}\ln(I_{PAS,T})+w_H\ln(I_{H,T})\Big]\end{aligned} \tag{40}$$

$$\begin{aligned}\frac{dJ}{d\alpha} = f_{\text{scal}}\Bigg[&w_\Phi\frac{1}{\Phi_{\text{rel}}}\frac{d(\Phi_{\text{rel}})}{d\alpha}\\ &+w_{PAS}\frac{1}{I_{PAS,T}}\frac{dI_{PAS,T}}{d\alpha}\\ &+w_H\frac{1}{I_{H,T}}\frac{dI_{H,T}}{d\alpha}\Bigg]\end{aligned} \tag{41}$$

2) For minimizing $\Phi_{\text{rel}} < 0$,

$$\begin{aligned}J = f_{\text{scal}}\Big[&-w_\Phi \ln(-\Phi_{\text{rel}})\\ &+w_{PAS}\ln(I_{PAS,T})+w_H\ln(I_{H,T})\Big]\end{aligned} \tag{42}$$

$$\begin{aligned}\frac{dJ}{d\alpha} = f_{\text{scal}}\Bigg[&w_\Phi\frac{1}{\Phi_{\text{rel}}}\frac{d(-\Phi_{\text{rel}})}{d\alpha}\\ &+w_{PAS}\frac{1}{I_{PAS,T}}\frac{dI_{PAS,T}}{d\alpha}\\ &+w_H\frac{1}{I_{H,T}}\frac{dI_{H,T}}{d\alpha}\Bigg]\end{aligned} \tag{43}$$

where “ln” is the natural logarithm, the weights w_Φ, w_{PAS} and w_H are constants ($w_\Phi + w_{PAS} + w_H = 1$), and f_{scal} is a scaling factor for the multi-objective function (chosen in this work as 10^3).

In this work, when considering a single objective function, the objective function value is considered directly in the optimization (i.e., the logarithmic function is not used). For example, when $w_\Phi = 1$, J is changed to $J = \Phi_{\text{rel}}$.

The computation of sensitivities is performed by automatic differentiation Farrell et al. (2013); Mitusch et al. (2019).

5 Numerical implementation of the optimization problem

The finite element method is implemented in the FEniCS platform (Logg et al., 2012), which is based on a high-level representation language used for the weak form that considers automatic differentiation, and on functionals later used for the finite element matrices assembly. The implementation of the topology optimization method is based on the dolfin-adjoint library (Farrell et al., 2013; Mitusch et al., 2019), which can automatically compute the adjoint model for the sensitivities. The optimization algorithm is given by IPOPT (Wächter and Biegler, 2006), which is based on a logarithmic barrier for the constraints (for search only in the feasible space). The penalty parameter of this logarithmic barrier is based on a line-search filter method, which avoids having to determine its exact value. The fluid flow problem in finite elements is given from a nonlinear weak form, considered by solving with the Newton-Raphson method, where MUMPS (Amestoy et al., 2001) is used for solving the arising linearized problems. The *mechanical dose shear-induced PAS* model is based on 3 linear differential equations – eqs. (27), (28) and (29) – and 1 non-linear differential equation – eq. (30) – while the hemolysis model is based on a single linear differential equation (Alonso and Silva, 2021). The nonlinear differential equation is solved similarly to the fluid flow problem, while the linear differential equation is directly given from a linear solver (LU solver). For the finite element modeling, Taylor-Hood elements are considered, and the design variable (pseudo-density) is assumed with linear interpolation.

Fig. 2 illustrates the implementation of the topology optimization method. The first step is the solution of the fluid flow problem with FEniCS, which is directly followed by the solutions of the hemolysis and thrombosis models. These executions that were initially performed for the finite element method in FEniCS are used to annotate (“store”) the operations and their order in dolfin-adjoint. Then, the IPOPT optimization loop can be started. The IPOPT algorithm communicates with dolfin-adjoint to compute the objective function, constraints and sensitivities: the sensitivities are automatically derived from the annotated models from FEniCS in dolfin-adjoint. The optimization loop is continued up to the specified tolerance (convergence criterion). In some numerical examples, the use of a Helmholtz pseudo-density filter is considered (Lazarov and Sigmund, 2010).

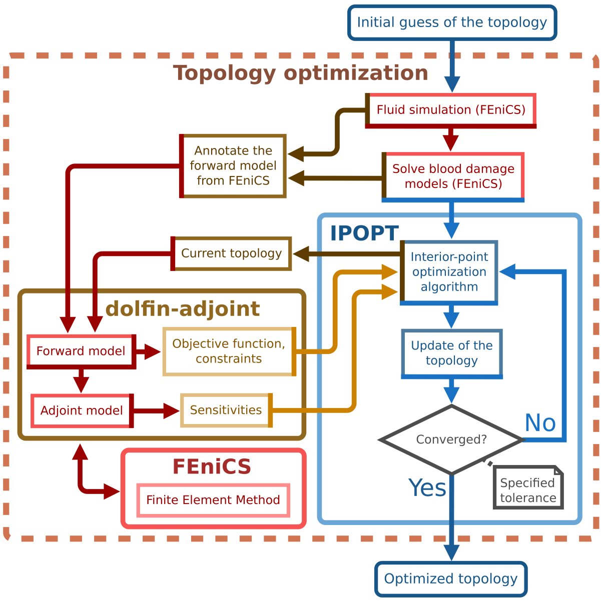

Fig. 2: Illustration of the numerical implementation.

An adjustment is considered for the sensitivities (of the objective function and constraint) by the volume of each element, similarly to when a Riesz map is considered in the sensitivity analysis, having the effect of leading to mesh-independency in the computed sensitivities. This effect is particularly interesting when considering non-uniform meshes, whereby the non-adjusted sensitivity distribution may be a seemingly less-smooth distribution, and may hinder the topology optimization process. In the case of the 2D swirl flow model, the elements of the 2D mesh can be viewed in 3D as *ring-shaped*, which means that there is a linear nonuniformity in the model when comparing lower and higher radii. In the case of a nodal design variable, the adjusted sensitivity can be computed as:

$$\left.\frac{dJ}{d\alpha}\right|_{\text{adjusted}} = \frac{1}{V_{\substack{\text{neighbor elements}\\ \text{of the node}}}} \frac{dJ}{d\alpha} \underbrace{\left[\frac{\sum_{\text{nodes}} V_{\substack{\text{neighbor elements}\\ \text{of the node}}}}{n_{\text{nodes}}} \right]}_{\text{Average neighbor elements' volume}} \tag{44}$$

where $V_{\substack{\text{neighbor elements}\\ \text{of the node}}}$ is the sum of the volumes of the neighbor elements that include a vertex/node in the mesh, and n_{nodes} is the number of vertices/nodes in the mesh. When considering the 2D swirl flow model, the volumes are computed while considering axisymmetry (i.e., that the elements are *ring-shaped*).

6 Numerical results

The fluid being considered in the numerical examples is blood, in which the non-Newtonian dynamic viscosity $\mu(\dot{\gamma}_{\text{m}})$ is given from eqs. (6) and (36), and the density (ρ) is given as 1056 kg/m^3 (Hinghofer-Szalkay and Greenleaf, 1987). The constants of the models presented in Sections 2.1 and 3.1 are presented in Table 1.

Table 1: Constants of the models presented in Sections 2.1 and 3.1 (Cho and Kenssey, 1991; Bird et al., 1987; Soares et al., 2013).

Variable	Value
a	1.5
n	0.22
λ	1.902 s
μ_0	0.056 Pa s
μ_∞	0.00345 Pa s
$C_{PAS,S}$	$1.5701 \times 10^{-7}\text{Pa}^{-1}\text{s}^{-2}$
$C_{PAS,sl}$	$1.4854 \times 10^{-7}\text{Pa}^{-\alpha_s}\text{s}^{-1}$
α_s	1.4854
α_t	1.4401
$C_{PAS,sr}$	$1.3889 \times 10^{-4}\text{Pa}^{-\delta_s}\text{s}^{\delta_s - 1}$
δ_s	0.5720
δ_t	0.5125

Aiming at better numerical conditioning for the computation of the weak form, the functionals (corresponding to the multi-objective function and the constraint) and the sensitivities (of the multi-objective function and the constraint), and also for aiming to improve the convergence rate, the Millimeters-Grams-Seconds (MMGS) unit system is considered, meaning that a 10^3 factor multiplies the length and mass units in the solution of the equations of the finite element method. The Newton-Raphson method convergence is set for absolute and relative tolerances of 10^{-10} and 10^{-9}, respectively. The convergence of the optimization is considered for a desired tolerance of 10^{-10} for the optimality error of the IPOPT barrier problem (Wächter and Biegler, 2006).

The external body forces are neglected in the numerical examples: $\rho \boldsymbol{f} = (0,\ 0,\ 0)$. The modeled solid material is considered with the same movement as the reference frame, meaning that $\boldsymbol{v}_{\text{mat}} = \boldsymbol{v}$. Moreso, κ_{min} is set as 0 $\text{kg}/(\text{m}^3\ \text{s})$. The initial guess for the topology (i.e., α) is set as a uniform distribution of $\alpha = f - 1\%$, where f is a fluid volume fraction that is specified, and 1% is to keep a small distance from the volume constraint. The plots of the optimized topologies assume the design variable (pseudo-density) values in the center of each finite element. Rotation in rpm is represented as n, and rotation in rad/s is represented as ω.

The post-processing of the pseudo-density (design variable) values in the optimized topologies is performed by separating the fluid part from the computational domain ($\alpha = 1$) in a separated mesh (i.e., in a *threshold* approach), and by smoothing the resulting mesh contour, aiming to ease *jagged mesh*-like effects (caused by the finite element discretization used during optimization) in the simulations of the optimized topologies (Fig. 3). All of the computed values, with the exception of the convergence curves, are computed in the post-processed meshes.

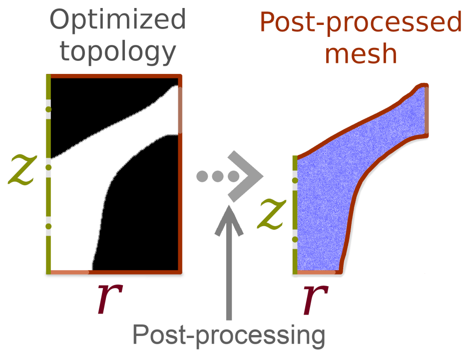

Fig. 3: Post-processing considered for the optimized topologies.

The Reynolds number is computed from the maximum of its local value. The local value is given as

$$\mathrm{Re}_{\mathrm{ext},\,\ell} = \frac{\mu(\dot{\gamma}_{\mathrm{m}})\,|\boldsymbol{v}_{\mathrm{abs}}|\,L}{\rho} \tag{45}$$

where the characteristic length (L) is set differently for the numerical examples: $L = 2r_{ext}$ (external diameter) in the 2D swirl flow examples (* "r_{ext}" corresponds to "R" in the first example), while $L = h_{in}$ (width of the inlet) in the 2D case.

The pressure head (H) is given as shown in eq. (46). When H is positive, H may be considered to characterize the capacity of pumping fluid. When H is negative, the inverse of the pressure head (i.e., the head loss, $H' = -H$) may be considered to characterize the energy loss inside the fluid flow device.

$$\begin{aligned} H = \frac{1}{Q}\Bigg[\int_{\Gamma_{\mathrm{in}}} \left(\frac{p}{\rho g} + \frac{|\boldsymbol{v}_{\mathrm{abs}}|^2}{2g}\right) \boldsymbol{v}\bullet\boldsymbol{n} 2\pi r d\Gamma_{\mathrm{in}} \\ + \int_{\Gamma_{\mathrm{out}}} \left(\frac{p}{\rho g} + \frac{|\boldsymbol{v}_{\mathrm{abs}}|^2}{2g}\right) \boldsymbol{v}\bullet\boldsymbol{n} 2\pi r d\Gamma_{\mathrm{out}}\Bigg] \end{aligned} \tag{46}$$

where $g = 9.8\ \mathrm{m/s^2}$ is the gravity acceleration.

In pump devices, the isentropic efficiency is a measure that can be used to characterize their efficiency (Rey Ladino, 2004; Sonntag and Borgnakke, 2013), and may be given as:

$$\eta_s = \frac{P_{ideal}}{P_{real}} = \frac{\Delta h_s}{P_f/\dot{m}} = \frac{gH}{P_f/\dot{m}} \tag{47}$$

where $\Delta h_s = gH$ is the specific enthalpy variation (specific work) of the corresponding ideal process (Sonntag and Borgnakke, 2013), $\dot{m} = \rho Q$ is the mass flow rate, and P_f is the fluid power, which is given by

$$P_f = \oint_{\Gamma} \boldsymbol{\omega}\bullet(\boldsymbol{r} \wedge \boldsymbol{v}_{\mathrm{abs}})\rho \boldsymbol{v}_{\mathrm{abs}}\bullet\boldsymbol{n} 2\pi r d\Gamma \tag{48}$$

The variations of static pressure Δp and total (*stagnation*) pressure Δp_T are computed for the Tesla blood pump rotor example, and are given as

$$\Delta p = \overline{p}_{out} - \overline{p}_{in} = \frac{\int_{\Gamma_{\mathrm{out}}} p 2\pi r d\Gamma_{\mathrm{out}}}{\int_{\Gamma_{\mathrm{out}}} 2\pi r d\Gamma_{\mathrm{out}}} - \frac{\int_{\Gamma_{\mathrm{in}}} p 2\pi r d\Gamma_{\mathrm{in}}}{\int_{\Gamma_{\mathrm{in}}} 2\pi r d\Gamma_{\mathrm{in}}} \tag{49}$$

$$\begin{aligned} \Delta p_T = \overline{p}_{T,out} - \overline{p}_{T,in} = & \frac{\int_{\Gamma_{\mathrm{out}}} \left(p + \frac{\rho|\boldsymbol{v}_{\mathrm{abs}}|^2}{2}\right) 2\pi r d\Gamma_{\mathrm{out}}}{\int_{\Gamma_{\mathrm{out}}} 2\pi r d\Gamma_{\mathrm{out}}} \\ & - \frac{\int_{\Gamma_{\mathrm{in}}} \left(p + \frac{\rho|\boldsymbol{v}_{\mathrm{abs}}|^2}{2}\right) 2\pi r d\Gamma_{\mathrm{in}}}{\int_{\Gamma_{\mathrm{in}}} 2\pi r d\Gamma_{\mathrm{in}}} \end{aligned} \tag{50}$$

When considering the Helmholtz pseudo-density filter, the design variable value is filtered (α_f) inside the whole computational domain (Ω), and then its value outside the design domain ($\Omega \setminus \Omega_\alpha$) is enforced as the previous value (α). Therefore, the variable $\alpha_{f,\mathrm{new}}$ is used in the equations, being given in function of the position ($\boldsymbol{s}$):

$$\alpha_{f,\mathrm{new}}(\boldsymbol{s}) = \begin{cases} \alpha_f, \text{ if } \boldsymbol{s} \in \Omega_\alpha \\ \alpha, \quad \text{if } \boldsymbol{s} \in \Omega \setminus \Omega_\alpha \end{cases} \tag{51}$$

Three numerical examples are presented, for: a Tesla blood pump (2D swirl flow model), a hydrocyclone-type device (2D swirl flow model) and a bypass graft (2D model).

For simplicity, in figures and tables, the values for w_Φ are not written in all of the cases, but may be calculated by $w_\Phi = 1 - w_{PAS} - w_H$ when not specified. Also, if w_{PAS} is not specified, $w_{PAS} = 0$, and, if w_H is not specified, $w_H = 0$.

6.1 Tesla blood pump

The first example considers the design of a Tesla-type blood pump, which has been previously considered for the hemolysis model in Alonso and Silva (2021). A Tesla-type pump is a bladeless continuous flow pump, being based on rotation and the boundary layer effect to pump the fluid (* In this work, for simplicity, this basic principle is referred to as *Tesla principle*). Some characteristics of *Tesla principle*-based devices in relation to conventional bladed pumps are less sensitivity to cavitation induced by vibration (Dodsworth, 2016), and less noise level due to the abscence of flow separation as in bladed pumps (Hasinger and Kehrt, 1963). When considering a Tesla-type pump as a VAD (Dorman et al., 1966; Hasinger and Kehrt, 1963; Izraelev et al., 2009), the nonpulsatile and continuous flow can help reduce blood damage, which is given by hemolysis and thrombosis, in these devices (Yu, 2015). The design domain considered in this work is shown in Fig. 4.

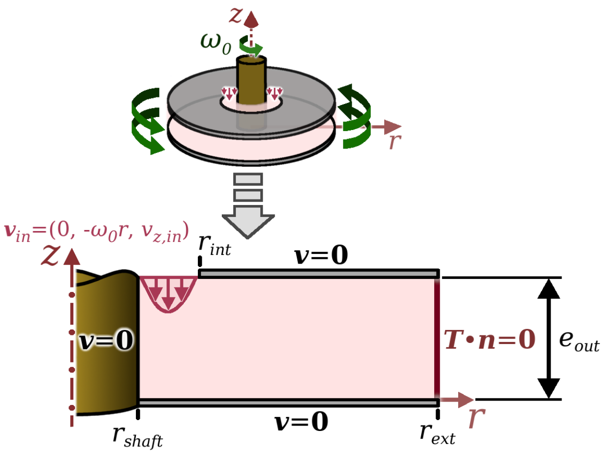

Fig. 4: Design domain considered for the Tesla blood pump.

The mesh is composed of 10,277 nodes and 20,240 elements, as shown in Fig. 5. The input parameters, geometric dimensions and material model parameters being considered in the design are shown in Table 2. The specified fluid volume fraction (f) is set as 30%.

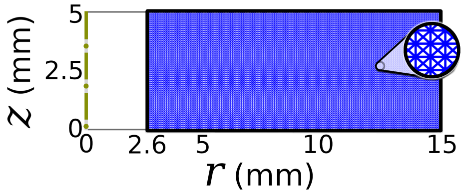

Fig. 5: Mesh considered in the design of the Tesla blood pump.

Table 2: Parameters considered for the topology optimization of the Tesla blood pump.

Input parameters	
Inlet flow rate (Q)	1.0 L/min
Wall rotation (n_0)	2,000 rpm
Inlet velocity profile	Parabolic
Dimensions	
r_{shaft}	2.6 mm
r_{int}	5 mm
e_{out}	5 mm
r_{ext}	15 mm
Material model parameters*	
$\kappa_{\max}$ ($\times 10^9 \mu_\infty$ (kg/(m^3 s)))	8.0
q	1.0
$\kappa_{PAS,\max}$ (s^{-1})	10^2

* The optimization considers a Helmholtz pseudo-density filter (Lazarov and Sigmund, 2010) to better stabilize the discrete optimized topologies, with a filter length parameter of 0.0543 mm.

The topology optimization results for the PAS index are shown in Fig. 6. Higher w_{PAS} values than the ones shown in Fig. 6 are not considered, due to convergence issues. The maximum local Reynolds number in the optimized topologies is 2.9×10^4. The transition Reynolds number is in the order of 10^6 in conventional pumps (Sabersky et al., 1971; Wu, 2007), meaning that 2.9×10^4 should correspond to laminar flow. As observed in Fig. 6, a tendency to create an inclined channel can be seen when higher PAS index (i.e., thrombosis) weights (w_{PAS}) are considered. Fig. 6a shows that the inclined channel topology is even better than the topology optimized for the relative energy dissipation ($w_\Phi = 1$). This lack of a Pareto-like behavior possibly means that the optimized topology for relative energy dissipation ($w_\Phi = 1$) is an easier local minimum for topology optimization, and the PAS index, even while being improved, coincidentaly induced a better local minimum for the relative energy dissipation, also improving the hemolysis index, the pressure head, the isentropic efficiency and the variations of static and total pressures. In the case of $w_{PAS} = 0.4$, by comparing with $w_\Phi = 1$, the improvements would be -4.7% (relative energy dissipation), -5.4% (PAS index), -12.0% (hemolysis index), +3.0% (pressure head), +2.5% (isentropic efficiency), +16.8% (static pressure head), and +14.2% (total pressure head).

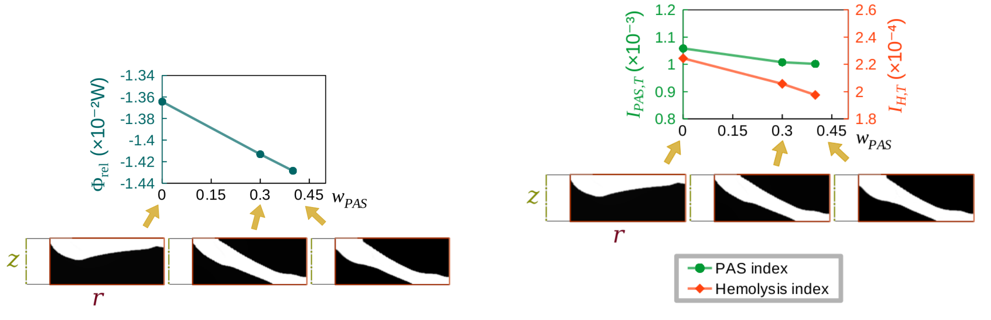

(a) Relative energy dissipation Φ_{rel}.

(b) PAS index $I_{PAS,T}$ and hemolysis index $I_{H,T}$.

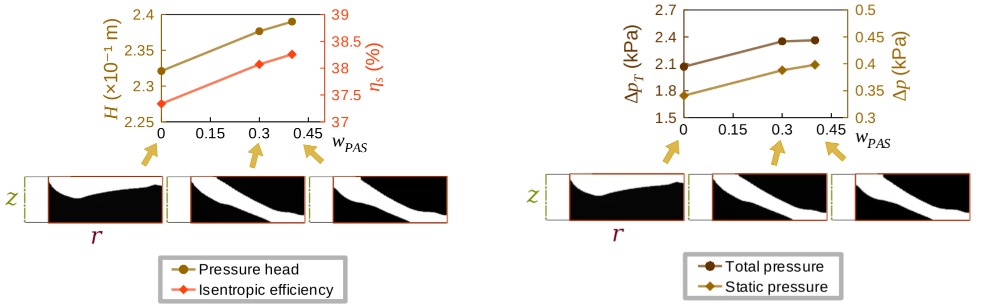

(c) Pressure head H and isentropic efficiency η_s.

(d) Variations of total pressure $\mathit{\Delta} p$ and static pressure $\mathit{\Delta} p_T$.

Fig. 6: Topology optimization results for the Tesla blood pump under different weights in the multi-objective function for the PAS index.

The topology optimization results for the hemolysis index are shown in Fig. 7. Note that the optimized topology for $w_H = 0.9$ is quite similar to the optimized topologies obtained for the PAS index (Fig. 6), such as the one for $w_{PAS} = 0.4$. In fact, the small differences in the optimized topologies led the computed variables to be even better for $w_H = 0.9$.

For reference, an additional case combining both hemolysis and thrombosis is also considered ($w_{PAS} = 0.1$, $w_H = 0.5$). This additional case is shown in Fig. 8. For comparing all of the optimized topologies, their relative values computed with respect to the reference design (Fig. 9) are shown in Table 3. As can be noticed, the worst result seems to be for $w_\Phi = 1$, which seems to indicate that the relative energy dissipation objective function induced a local minimum. This type of local minimum could possibly be avoided by taking blood damage into account in topology optimization, as can be seen from the values for the other optimized topologies. Note that the hemolysis index is significantly smaller in the optimized topologies, which is mainly due to the absence of a sharp edge that is present in the straight disks topology (Fig. 9). The combined result ($w_{PAS} = 0.1$ and $w_H = 0.5$), from Table 3, shows slightly better hemolysis and thrombosis with respect to $w_{PAS} = 0.4$ and $w_H = 0.7$, showing that it is possible to consider both effects in topology optimization. However, the best result is the one for $w_H = 0.9$, which is better than all of the other optimized topologies in all of the values. Thus, from Table 3, the best optimized topologies seem to be the one for $w_H = 0.9$, followed by the one for the combined case ($w_{PAS} = 0.1$ and $w_H = 0.5$).

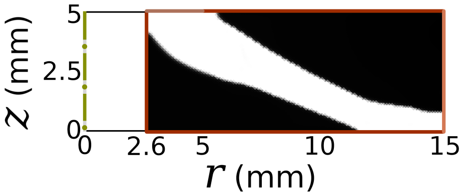

Fig. 8: Optimized topology for the combined case ($w_{PAS} = 0.1$ and $w_H = 0.5$) for the Tesla blood pump.

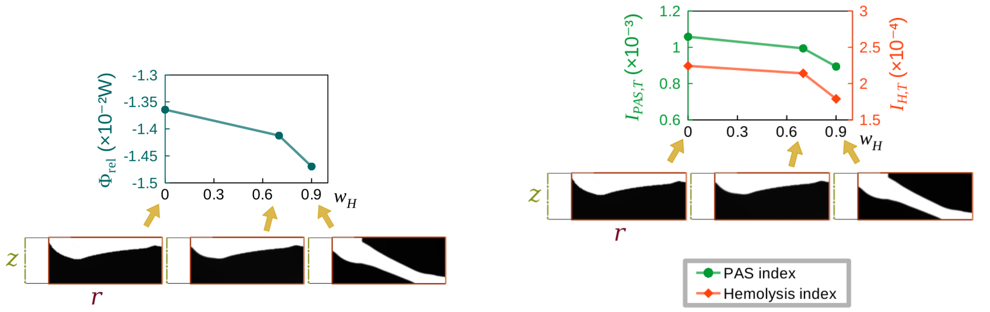

(a) Relative energy dissipation Φ_{rel}.

(b) PAS index $I_{PAS,T}$ and hemolysis index $I_{H,T}$.

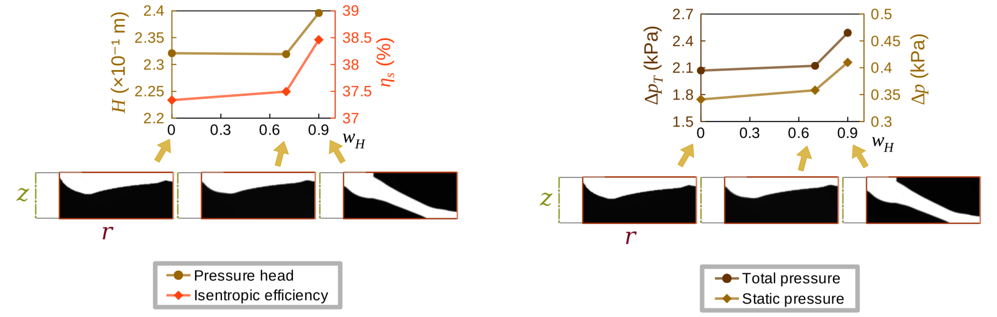

(c) Pressure head H and isentropic efficiency η_s.

(d) Variations of total pressure Δp and static pressure Δp_T.

Fig. 7: Topology optimization results for the Tesla blood pump under different weights in the multi-objective function for the hemolysis index.

Table 3: Relative comparison of the optimized topologies for the Tesla blood pump with the reference design (Fig. 9).

Designs	Φ_{rel}	$I_{PAS,T}$	$I_{H,T}$	H	η_s	Δp_s	Δp_T
$w_\Phi = 1$	+2.0%	-7.7%	-46.3%	-2.2%	-1.6%	-6.6%	+5.2%
$w_{PAS} = 0.3$	-1.5%	-12.1%	-50.8%	+0.1%	+0.3%	+6.3%	+19.5%
$w_{PAS} = 0.4$	-2.6%	-12.6%	-52.7%	+0.7%	+0.8%	+9.1%	+20.1%
$w_H = 0.7$	-1.4%	-13.3%	-48.8%	-2.3%	-1.2%	-1.9%	+7.9%
$w_H = 0.9$	-5.6%	-22.0%	-57.2%	+1.0%	+1.4%	+12.3%	+26.6%
$w_{PAS} = 0.1$ and $w_H = 0.5$	-3.8%	-13.8%	-53.0%	+0.5%	+0.9%	+10.2%	+19.6%

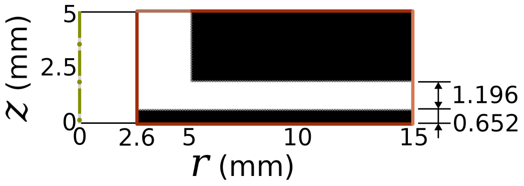

Fig. 9: Straight disks reference topology for the Tesla blood pump.

To show an example of how the topology optimization progresses, the convergence curve of the topology optimization of the Tesla blood pump for the combined case ($w_{PAS} = 0.1$ and $w_H = 0.5$) is shown in Fig. 10. The convergence curve behaves similarly for the other optimized topologies for the Tesla blood pump.

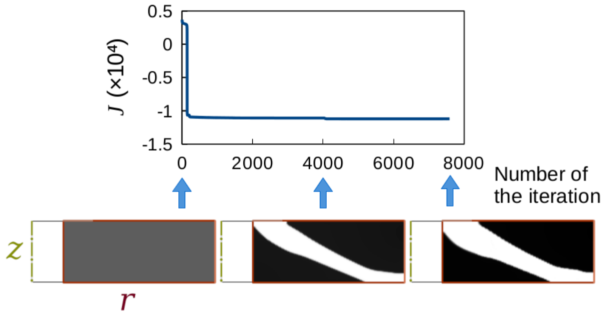

Fig. 10: Convergence curve of the topology optimization of the Tesla blood pump for the combined case ($w_{PAS} = 0.1$ and $w_H = 0.5$).

The simulation results for the optimized topologies, for the combined case ($w_{PAS} = 0.1$ and $w_H = 0.5$) and for $w_H = 0.9$, are shown in Fig. 11. From the local hemolysis index (I_H) plots, it can be noticed that hemolysis is present at a greater intensity near the outlet. This, however, does not mean that the hemolysis near the inlet is zero (from the color scale), meaning that the hemolysis near the inlet is much smaller than that near the outlet. The local PAS index (I_{PAS}) plot is more distributed along the computational domain than the hemolysis index. The pressure (p) in the middle part of the optimized topologies shows an approximately linear increase, while the radial-axial velocity (v_r, v_z) is concentrated mainly near the lower interface, although there is a smaller flow near the upper surface. The relative tangential velocity (v_θ) shows that, as the radius coordinate (r) increases, the fluid gets slower in the θ direction in the middle of the "channel", which is consistent, since the fluid is being dragged near the walls. By comparing both optimized topologies, from Figs. 11a ($w_{PAS} = 0.1$ and $w_H = 0.5$) and 11b ($w_H = 0.9$), it can be noticed that the main difference is the initial curvature, which is more apparent in Fig. 11b ($w_H = 0.9$) than in Fig. 11a ($w_{PAS} = 0.1$ and $w_H = 0.5$). This seems to ease the change in flow direction (lower shear stresses), leading to lower hemolysis ($I_{H,T}$) and thrombosis ($I_{PAS,T}$) – see Table 3.

The non-Newtonian viscosity distributions are also shown in Fig. 11. Note that the non-Newtonian effect is more pronounced closer to the inlet and farther from the walls. This is due to the increase in shear stress when close to walls, which is caused by the effect of the rotation and, consequently, by the *Tesla principle*.

Since both hemolysis and thrombosis increase near the outlet walls, a relation between them can be perceived. This relation is given from the shear stress, which is present in their respective equations, namely eq. (33) and eqs. (27), (28), (29) and (30). However, as shown in Fig. 11, hemolysis and thrombosis still do not feature exactly the same behavior, due to the different coefficients and other effects present in the thrombosis modeling (platelet sensitization and stress rate effects).

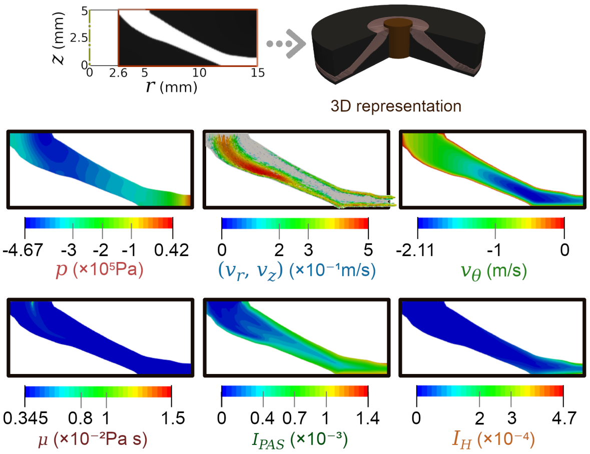

(a) Optimized topology for the combined case ($w_{PAS} = 0.1$ and $w_H = 0.5$).

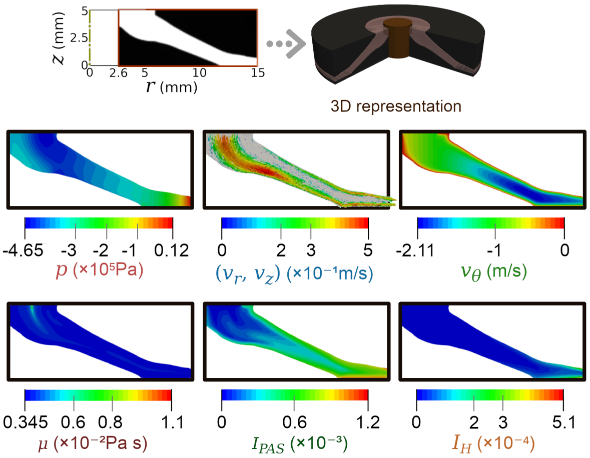

(b) Optimized topology for $w_H = 0.9$.

Fig. 11: Optimized topology, pressure, velocity, dynamic viscosity, PAS index, and hemolysis index for the optimized Tesla blood pump for two different cases.

6.2 Hydrocyclone-type device

The second example considers the design of a hydrocyclone-type device. This type of device is different from a real hydrocyclone device, because it models a flow with a single phase (instead of considering two phases) entering with a rotation (ω_{in}) from a single inlet towards a single outlet. The design domain considered for the 2D swirl flow model is selected as shown in Fig. 12. The solid material distribution is considered to be optimized for the static walls ($\omega_0 = 0$ rad/s).

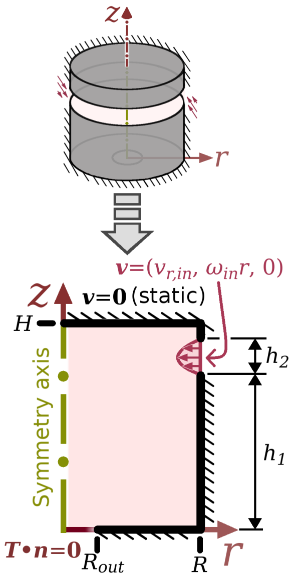

Fig. 12: Design domain considered for the hydrocyclone-type device.

The mesh is composed of 19,401 nodes and 38,400 elements (see Fig. 13). The input parameters, geometric dimensions and material model parameters considered in the design are shown in Table 4. The specified fluid volume fraction (f) is set as 30%.

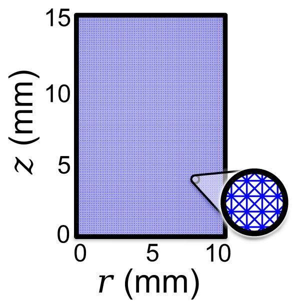

Fig. 13: Mesh considered in the design of the hydrocyclone-type device.

Table 4: Parameters considered for the topology optimization of the hydrocyclone-type device.

Input parameters	
Inlet flow rate (Q)	0.05 L/min
Wall rotation (n_0)	0 rpm
Inlet rotation (n_{in})	20 rpm
Inlet velocity profile	Parabolic
Dimensions	
H	15 mm
R	10 mm
h_1	11 mm
h_2	3 mm
Material model parameters*	
$\kappa_{\max}$ ($\times 10^7 \mu_\infty$ (kg/(m^3 s)))	8.0
q	1.0
$\kappa_{PAS,\max}$ (s^{-1})	10^3

* The optimization considers a Helmholtz pseudo-density filter (Lazarov and Sigmund, 2010) to better stabilize the discrete optimized topologies, with a filter length parameter of 0.0625 mm.

In this numerical example, some of the factors that influence the topology optimization for hemolysis and thrombosis are illustrated separately. In the optimized topologies, the maximum local Reynolds number is 177, which means that the flow is laminar. Fig. 14 shows the effect of the additional penalization from the thrombosis model ($\kappa_{PAS,\max}$), by considering $w_{PAS} = 0.5$. The corresponding contours are shown enlarged in Fig. 15. The optimized topologies mainly show slight differences near the outlet, and near the solid material that is near the rotation axis. Particularly, the optimized topology for $\kappa_{PAS,\max} = 10^3$ s^{-1} is slightly more inclined to the right and is straighter near the outlet, with respect to the optimized topology for $\kappa_{PAS,\max} = 0.1$ s^{-1}. The fact that it is straighter near the outlet (with respect to the optimized topology for $\kappa_{PAS,\max} = 0.1$) seems contribute to further reducing the low velocity values that appear near the wall next to the outlet (thus helping to reduce thrombosis), and the small differences with respect to the optimized topology for $\kappa_{PAS,\max} = 1$ eventually led to a slight increase in the velocity gradients near the start of the straighter part of the outlet, thus helping to slightly increase hemolysis alongside the small curvature changes in the overall topology. These small differences seem to lead to slightly increased velocity gradients, worsening the relative energy dissipation, while the head loss is reduced from a straighter fluid flow velocity exiting the fluid flow device. From Fig. 14, it can be noticed that higher $\kappa_{PAS,\max}$ values lead to worse relative energy dissipation (Fig. 14a), better head loss (Fig. 14a) and worse hemolysis (Fig. 14b). However, there is some improvement in thrombosis (Fig. 14b).

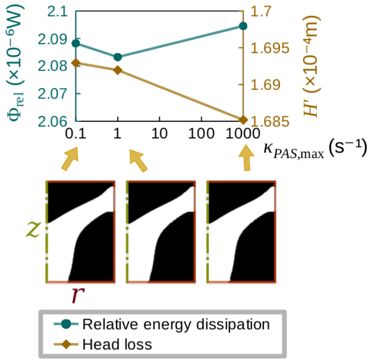

(a) Relative energy dissipation Φ_{rel} and head loss H'.

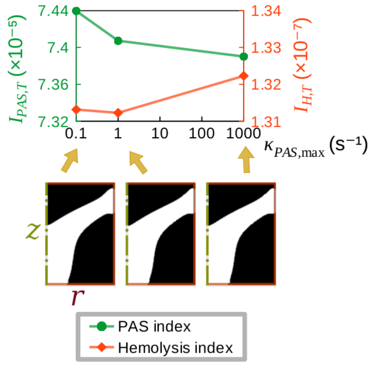

(b) PAS index I_{PAS} and hemolysis index I_H.

Fig. 14: Topology optimization results for the hydrocyclone-type device for $w_{PAS} = 0.5$, considering different $\kappa_{PAS,\max}$ values.

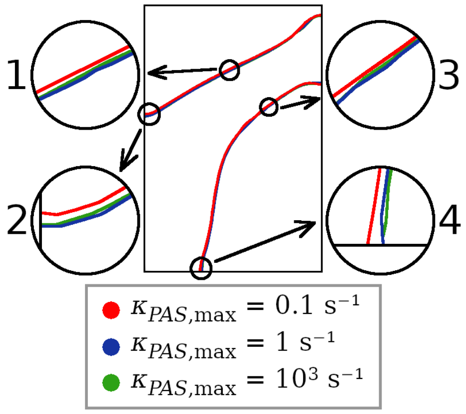

Fig. 15: Contours of the optimized topologies from Fig. 14.

By considering $\kappa_{PAS,\max} = 10^3$ s^{-1}, which showed the best PAS index value in Fig. 14b, the effect of the thrombosis weight (w_{PAS}) is evaluated. The results are shown in Fig. 16 and the corresponding contours are shown enlarged in Fig. 17. In Fig. 16b, it can be noticed that there may be induction of local minima depending on the w_{PAS} value, such as for $w_{PAS} = 0.3$, which improved hemolysis while worsening thrombosis. In Fig. 16b, it can be noticed that overprioritizing thrombosis, such as in $w_{PAS} = 0.9$, may lead to significantly worse relative energy dissipation and head loss. In particular, the main aspect of the optimized topology for $w_{PAS} = 0.9$ is that it is more inclined to the right than the other optimized topologies, which means that the fluid flow path is slightly larger (due to the axisymmetric volume) than the other optimized topologies (more inclined to the left), leading to a higher energy dissipation. The hemolysis is also higher, which is possibly due to the upper solid material boundary (located lower than the other topologies).

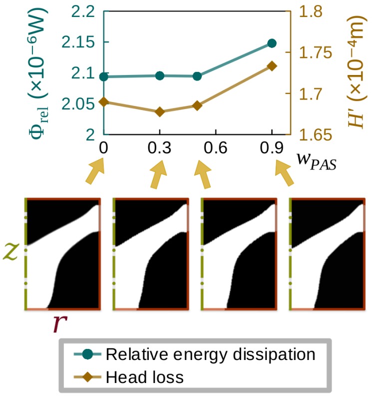

(a) Relative energy dissipation Φ_{rel} and head loss H'.

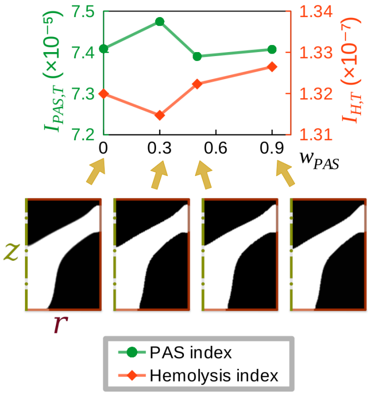

(b) PAS index I_{PAS} and hemolysis index I_H.

Fig. 16: Topology optimization results for the hydrocyclone-type device for different w_{PAS} values ($\kappa_{PAS,\max} = 10^3\ \text{s}^{-1}$).

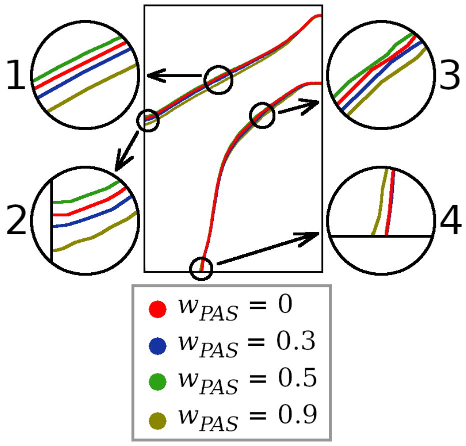

Fig. 17: Contours of the optimized topologies from Fig. 16.

The effect of the hemolysis weight (w_H) is shown in Fig. 18. The effect is similar to the one shown for w_{PAS} (Fig. 16) and the corresponding contours are shown enlarged in Fig. 19. However, a better local minimum was induced when $w_H = 0.5$ (better hemolysis and thrombosis), and a worse local minimum was induced when $w_H = 0.9$ (worse hemolysis and thrombosis). The optimized topology for $w_H = 0.9$ shows a more inclined path near the outlet, which reduces the fluid volume flowing near the outlet (noting that the fluid volume is axisymmetric), possibly increasing the corresponding velocity gradients and, therefore, hemolysis and thrombosis.

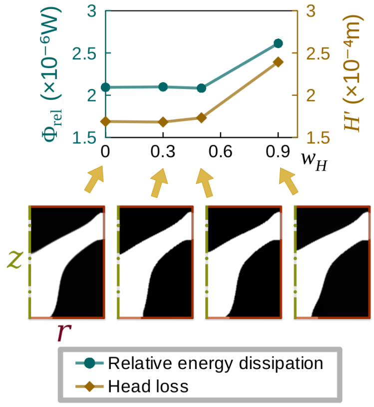

(a) Relative energy dissipation Φ_{rel} and head loss H'.

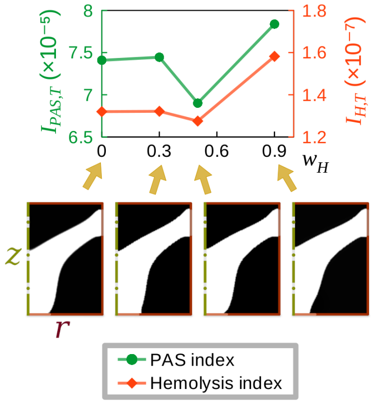

(b) PAS index I_{PAS} and hemolysis index I_H.

Fig. 18: Topology optimization results for the hydrocyclone-type device for different w_H values.

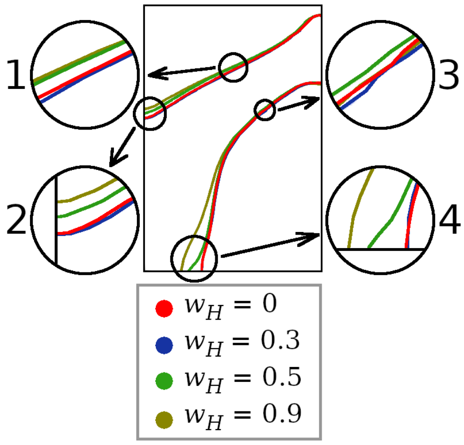

Fig. 19: Contours of the optimized topologies from Fig. 18.

An additional analysis is performed by combining hemolysis ($w_H = 0.3$) and thrombosis ($w_{PAS} = 0.3$) in the same multi-objective function. Figs. 20 and 21 show a comparison between the optimized topologies for $w_\Phi = 1$, $w_{PAS} = 0.3$, $w_H = 0.3$ and "$w_{PAS} = 0.3$ and $w_H = 0.3$". It can be seen that considering both hemolysis and thrombosis may lead to a better optimized topology for both quantities. In particular, the optimized topology for "$w_{PAS} = 0.3$ and $w_H = 0.3$" shows a curve near the outlet, which reduced thrombosis, and the upper part of the "channel" is located at a higher position.

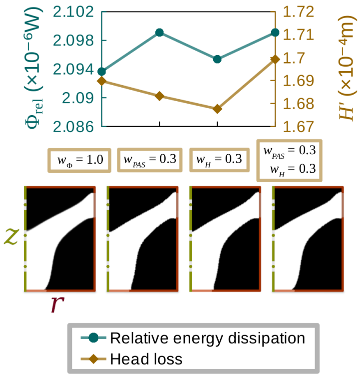

(a) Relative energy dissipation Φ_{rel} and head loss H'.

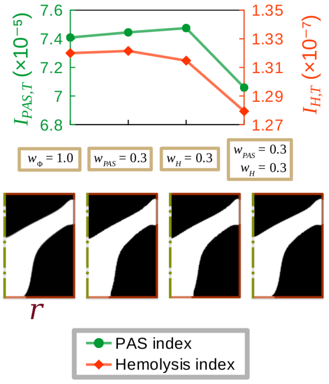

(b) PAS index I_{PAS} and hemolysis index I_H.

Fig. 20: Topology optimization results for the hydrocyclone-type device considering w_{PAS} and w_H.

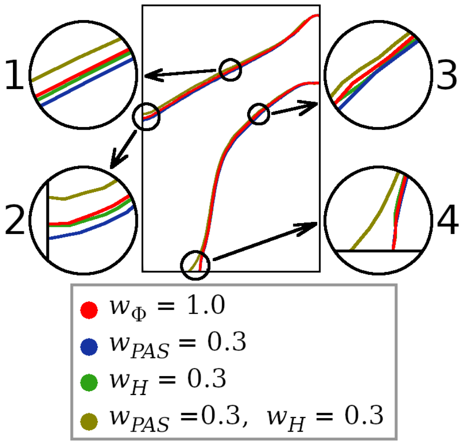

Fig. 21: Contours of the optimized topologies from Fig. 20.

Overall, the best result is the one for $w_H = 0.5$. Nonetheless, the result for $w_{PAS} = 0.5$ ($\kappa_{PAS,\max} = 10^3\ \mathrm{s}^{-1}$) is not far. The convergence curve for $w_{PAS} = 0.5$ ($\kappa_{PAS,\max} = 10^3\ \mathrm{s}^{-1}$) is shown in Fig. 22.

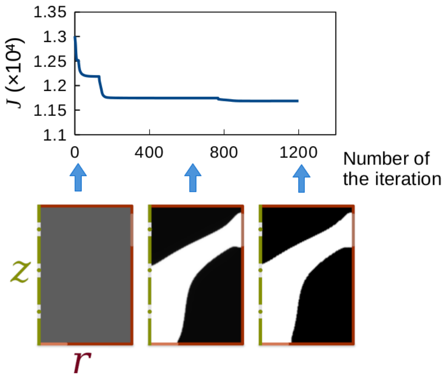

Fig. 22: Convergence curve of the topology optimization of the hydrocyclone-type device ($w_{PAS} = 0.5$, $\kappa_{PAS,\max} = 10^3\ \mathrm{s}^{-1}$).

The optimized topology for $w_{PAS} = 0.5$ ($\kappa_{PAS,\max} = 10^3\ \mathrm{s}^{-1}$) is simulated in Fig. 23. As can be seen, the tangential velocity (v_θ) is dissipated/converted to radial-axial velocity (v_r, v_z) in the first part of the optimized topology from the inlet. The non-Newtonian effect can be observed mainly near the middle of the fluid flow cross-section. The non-Newtonian viscosity $\mu(\dot{\gamma}_\mathrm{m})$ is observed to slightly rise next to the outlet due to the formation of a small stagnated zone. The plots of local PAS index (I_{PAS}) and local hemolysis index (I_H) show similar behaviors in the sense that both quantities are small near the inlet and increase as the fluid flows through the device. However, the local PAS index I_{PAS} is more widely spread towards the outlet. It can also be noted that the local PAS index (I_{PAS}) and local hemolysis index (I_H) plots can be viewed as maps of the potential blood damage that can happen to blood flow.

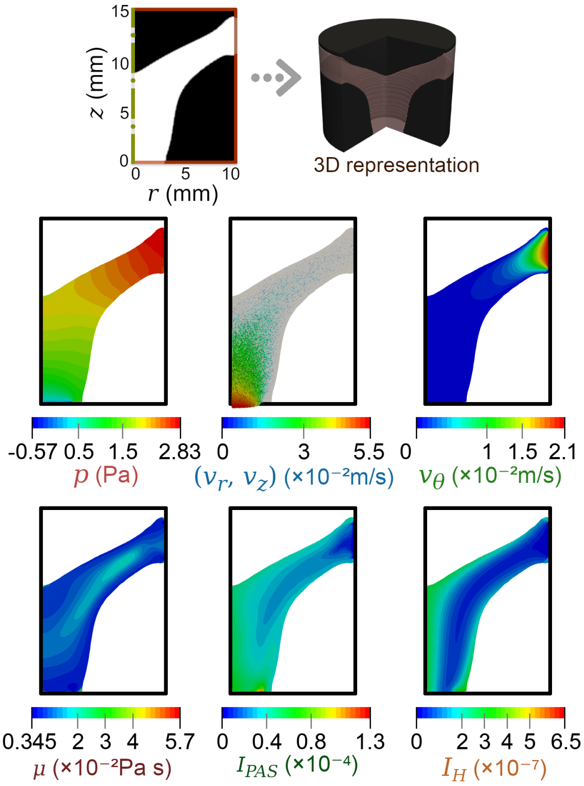

Fig. 23: Optimized topology, pressure, velocity, dynamic viscosity, PAS index and hemolysis index for the optimized hydrocyclone-type device ($w_{PAS} = 0.5$, $\kappa_{PAS,\max} = 10^3\ \mathrm{s}^{-1}$).

6.3 Bypass graft

The third example is the design of a bypass graft, considered through a 2D model. A bypass graft is used to allow blood to bypass blocked coronary arteries, to restore the normal blood flow. The design of some bypass configurations has already been previously evaluated for shape optimization (Abraham et al., 2005) and topology optimization by the *level-set approach* (Zhang and Liu, 2015), by considering an energy dissipation objective function. In this work, a similar bypass configuration is considered for topology optimization by the *pseudo-density approach*, while also considering hemolysis and thrombosis in the optimization process. The computational domain is shown in Fig. 24, where the design domain does not include the inlet and outlet channels (which would represent the arteries). Since this configuration is non-rotating, it does not include any rotation ($\omega = 0$ rad/s, $\omega_0 = 0$ rad/s).

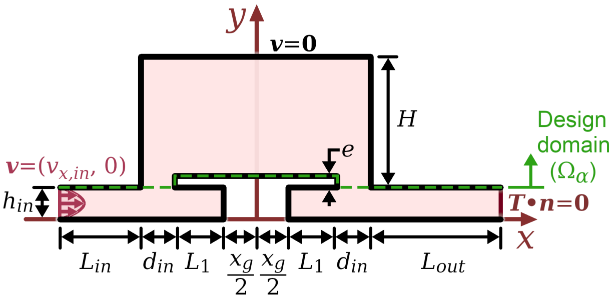

Fig. 24: Design domain considered for the bypass graft.

The mesh is unstructured, composed of 10,815 nodes and 20,888 elements (see Fig. 25). The input parameters, dimensions of the computational domain, and material model parameters used are shown in Table 5. The specified fluid volume fraction (f) is set as 35.3%.

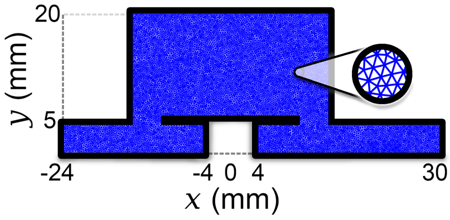

Fig. 25: Mesh considered in the design of the bypass graft.

Table 5: Parameters considered for the topology optimization of the bypass graft.

Input parameters	
Inlet flow rate (Q)	5.0 mL/min*
Inlet velocity profile	Parabolic
Dimensions	
H	20 mm
h_{in}	4 mm
r_i	30 mm
L_{in}	10 mm
L_{out}	16 mm
d_{in}	4 mm
L_1	6 mm
x_g	8 mm
e	1.5 mm
Material model parameters**	
$\kappa_{\max}$ ($\times 10^7 \mu_\infty$ (kg/(m^3 s)))	8.0
q	0.1
$\kappa_{PAS,\max}$ (s^{-1})	10^3

* The flow rate is computed assuming that the width of the inlet (h_{in}) corresponds to an "inlet diameter" (in 3D).
** The optimization considers a Helmholtz pseudo-density filter (Lazarov and Sigmund, 2010) to better stabilize the discrete optimized topologies, with a filter length parameter of 0.315 mm.

The bypass configuration is considered at a low maximum Reynolds number (6.4), which corresponds to laminar flow. The topology optimization resulted in one optimized topology for $w_\Phi = 1$, while the optimized topology for $w_{PAS} = 0.9$ and the optimized topology for $w_H = 0.9$ resulted the same (Fig. 26). The computed values in both topologies are shown in Table 6. As can be noticed, the optimized topology for $w_{PAS} = 0.9$ (or $w_H = 0.9$) is better for hemolysis and thrombosis than the optimized topology for $w_\Phi = 1.0$ – i.e., the energy dissipation is slightly worse (0.9% higher), the thrombosis is slightly better (2.6% lower), the hemolysis is slightly better (1.8% lower), and the head loss is slightly worse (1.0% higher).

Table 6: Computed values in the optimized topologies for the bypass design.

Designs	Φ_{rel} ($\times10^{-4}$ W/m)	$I_{PAS,T}$ ($\times10^{-5}$ 1/m)	$I_{H,T}$ ($\times10^{-8}$ 1/m)	H' ($\times10^{-4}$ m)
$w_\Phi = 1$	1.13	7.17	9.89	3.12
$w_{PAS} = 0.9$ (or $w_H = 0.9$)	1.14	6.98	9.71	3.15

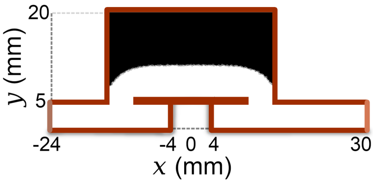

(a) For $w_\Phi = 1$.

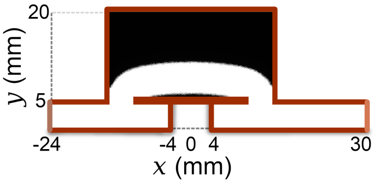

(b) For $w_H = 0.9$ or $w_{PAS} = 0.9$.

Fig. 26: Optimized topologies for the bypass graft.

The convergence curve for the optimized topology for $w_{PAS} = 0.9$ is shown in Fig. 27.

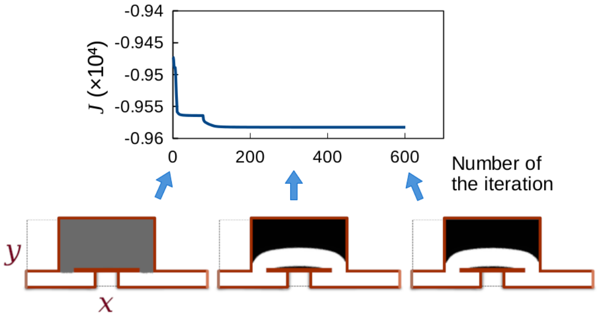

Fig. 27: Convergence curve of the topology optimization of the bypass graft ($w_{PAS} = 0.5$).

Both optimized topologies are simulated in Fig. 28. There is not much difference in the fluid flow behavior in either case, but the slightly dettached channel (Fig. 28b) leads to a smaller change in flow direction, which, in turn, reduces velocity gradients and improves hemolysis and thrombosis. This, however, worsens the energy dissipation (and the head loss), because the flow has to undergo a slightly larger path, which dissipates slightly more energy. The dynamic viscosity plots show that the non-Newtonian behavior is more significant in the middle of the flow cross-section and also inside the “stagnated flow zones” (indicated by L_1 in Fig. 24).

7 Conclusions

In this work, a formulation for considering a thrombosis model in topology optimization is presented, which was not performed in previous works. The thrombosis model consists in solving a set of differential equations adapted in this work for topology optimization (*mechanical dose shear-induced PAS* model). The sensitivity is obtained by combining the sensitivity from each weak form, which is automated by using the dolfin-adjoint library.

Three examples are shown: Tesla blood pump (2D swirl flow model), hydrocyclone-type device (2D swirl flow model) and bypass graft (2D model). The proposed additional penalization term (κ_{PAS}) is shown to improve thrombosis, even at the cost of hemolysis, which shows that, although hemolysis and thrombosis are closely related from the presence of the shear stress in their respective models, they have other effects and non-linearities which may even result in opposite behaviors in topology optimization. Furthermore, the non-linearities of the hemolysis and thrombosis models may lead to better or worse local minima when considering higher weights in the multi-objective function. A combination of both hemolysis and thrombosis in the optimization seems to be able to yield better results, although some local minima from considering only one of them may possibly achieve a better optimized topology. In terms of optimized topologies, in the Tesla blood pump example, the inclusion of hemolysis and/or thrombosis leads to the formation of *inclined disk*-like topologies; in the bypass graft case, the inclusion of hemolysis or thrombosis leads to the formation of a small “curve” in the middle zone of the computational domain.

As future work, some suggestions are to consider other blood damage models, thermal effects, turbulence and other flow machine designs.

8 Replication of results

The descriptions of the formulation, the numerical implementation and the numerical results contain all the

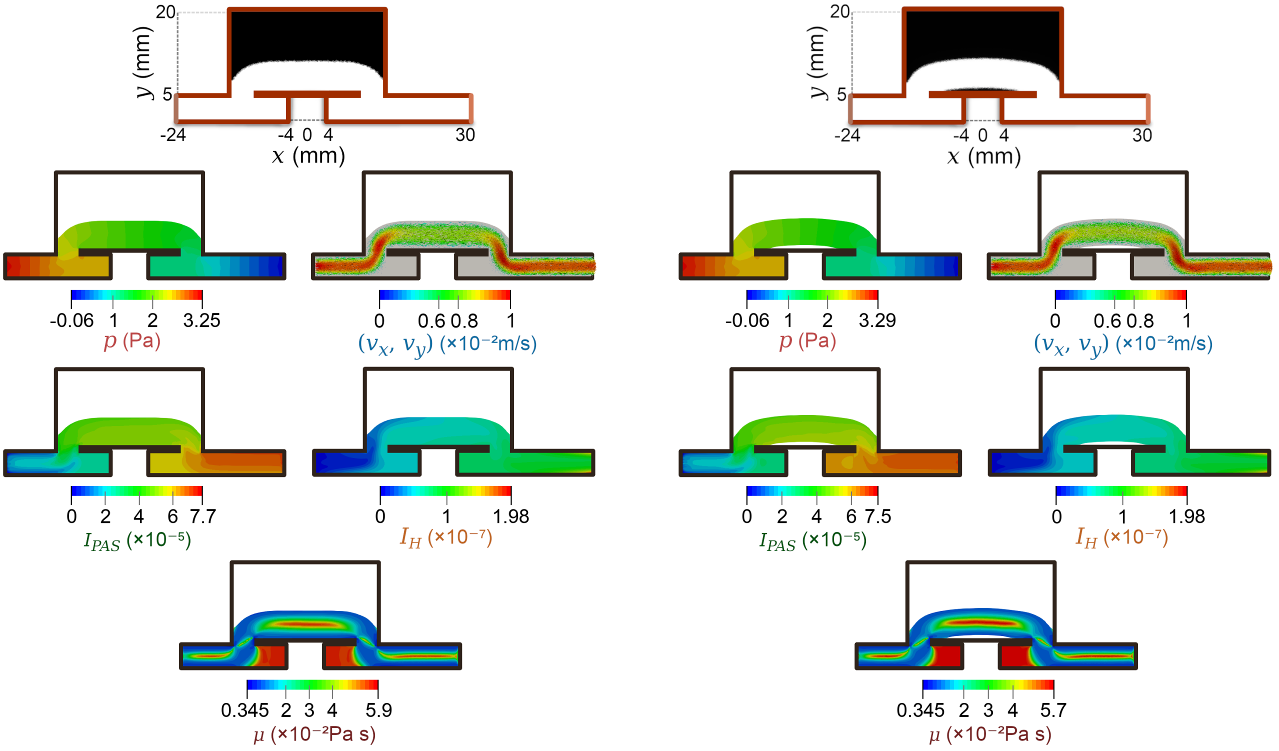

(a) For $w_{\Phi} = 1$.

(b) For $w_H = 0.9$ or $w_{PAS} = 0.9$.

Fig. 28: Optimized topology, pressure, velocity, PAS index, hemolysis index and dynamic viscosity for the optimized bypass grafts.

necessary information for reproducing the results of this article. Also, the tutorials/examples present in `http://www.dolfin-adjoint.org` may help with the implementation.

Funding information This research was partly supported by CNPq (Brazilian National Research Council) and FAPESP (São Paulo Research Foundation). The authors thank the supporting institutions. The first author thanks the financial support of FAPESP under grant 2017/27049-0. The second author thanks the financial support of CNPq (National Council for Research and Development) under grant 302658/2018-1 and of FAPESP under grant 2013/24434-0. The authors also acknowledge the support of the RCGI (Research Centre for Gas Innovation), which is hosted by the University of São Paulo (USP) and sponsored by FAPESP (2014/50279-4) and Shell Brazil.

Compliance with ethical standards

Conflict of interest The authors declare that they have no conflict of interest.

References

Abraham F, Behr M, Heinkenschloss M (2005) Shape optimization in steady blood flow: a numerical study of non-newtonian effects. Computer methods in biomechanics and biomedical engineering 8(2):127–137

Alemu Y, Bluestein D (2007) Flow-induced platelet activation and damage accumulation in a mechanical heart valve: numerical studies. Artificial organs 31(9):677–688

Alexandersen J, Andreasen CS (2020) A review of topology optimisation for fluid-based problems. Fluids 5(1):29

Alonso DH, Silva ECN (2021) Topology optimization for blood flow considering a hemolysis model. Structural and Multidisciplinary Optimization 63(5):2101–2123, DOI 10.1007/s00158-020-02806-x, URL `https://doi.org/10.1007%2Fs00158-020-02806-x`

Alonso DH, de Sá LFN, Saenz JSR, Silva ECN (2019) Topology optimization based on a two-dimensional swirl flow model of tesla-type pump devices. Computers & Mathematics with Applications 77(9):2499 – 2533, DOI https://doi.org/10.1016/j.camwa.2018.12.035, URL http://www.sciencedirect.com/science/article/pii/S0898122118307338

Alonso DH, Saenz JSR, Silva ECN (2020) Non-newtonian laminar 2d swirl flow design by the topology optimization method. Structural and Multidisciplinary Optimization 62(1):299–321, DOI https://doi.org/10.1007/s00158-020-02499-2, URL https://link.springer.com/article/10.1007%2Fs00158-020-02499-2

Amestoy PR, Duff IS, Koster J, L'Excellent JY (2001) A fully asynchronous multifrontal solver using distributed dynamic scheduling. SIAM Journal on Matrix Analysis and Applications 23(1):15–41

Antaki JF, Ghattas O, Burgreen GW, He B (1995) Computational flow optimization of rotary blood pump components. Artificial Organs 19(7):608–615

Apel J, Paul R, Klaus S, Siess T, Reul H (2001) Assessment of hemolysis related quantities in a microaxial blood pump by computational fluid dynamics. Artificial Organs 25(5):341–347, DOI 10.1046/j.1525-1594.2001.025005341.x, URL https://onlinelibrary.wiley.com/doi/abs/10.1046/j.1525-1594.2001.025005341.x, https://onlinelibrary.wiley.com/doi/pdf/10.1046/j.1525-1594.2001.025005341.x

Arora D, Behr M, Pasquali M (2004) A tensor-based measure for estimating blood damage. Artificial Organs 28(11):1002–1015

Arora D, Behr M, Pasquali M (2012) Errata. Artificial Organs 36(5):500–500, DOI 10.1111/j.1525-1594.2012.01491.x, URL https://onlinelibrary.wiley.com/doi/abs/10.1111/j.1525-1594.2012.01491.x, https://onlinelibrary.wiley.com/doi/pdf/10.1111/j.1525-1594.2012.01491.x

Bagot CN, Arya R (2008) Virchow and his triad: a question of attribution. British Journal of Haematology 143(2):180–190, DOI 10.1111/j.1365-2141.2008.07323.x, URL https://onlinelibrary.wiley.com/doi/abs/10.1111/j.1365-2141.2008.07323.x, https://onlinelibrary.wiley.com/doi/pdf/10.1111/j.1365-2141.2008.07323.x

Barthes-Biesel D, Rallison J (1981) The time-dependent deformation of a capsule freely suspended in a linear shear flow. Journal of Fluid Mechanics 113:251–267

Behbahani M, Behr M, Hormes M, Steinseifer U, Arora D, CORONADO O, Pasquali M (2009) A review of computational fluid dynamics analysis of blood pumps. European Journal of Applied Mathematics 20:363 – 397

Bird RB, Armstrong RC, Hassager O (1987) Dynamics of polymeric liquids, Volume 1: Fluid mechanics, 1st edn. John Wiley & Sons

Borrvall T, Petersson J (2003) Topology optimization of fluids in stokes flow. International Journal for Numerical Methods in Fluids 41(1):77–107, DOI 10.1002/fld.426, URL http://dx.doi.org/10.1002/fld.426

Brass LF (2003) Thrombin and platelet activation. Chest 124(3):18S–25S

Cheng R, Lai YG, Chandran KB (2004) Three-dimensional fluid-structure interaction simulation of bileaflet mechanical heart valve flow dynamics. Annals of biomedical engineering 32(11):1471–1483

Cho YI, Kenssey KR (1991) Effects of the non-newtonian viscosity of blood on flows in a diseased arterial vessel. part 1: Steady flows. Biorheology 28:241–262

Chopard B, de Sousa DR, Lätt J, Mountrakis L, Dubois F, Yourassowsky C, Van Antwerpen P, Eker O, Vanhamme L, Perez-Morga D, et al. (2017) A physical description of the adhesion and aggregation of platelets. Royal Society open science 4(4):170219

Consolo F, Valerio L, Brizzola S, Rota P, Marazzato G, Vincoli V, Reggiani S, Redaelli A, Fiore G (2016) On the use of the platelet activity state assay for the in vitro quantification of platelet activation in blood recirculating devices for extracorporeal circulation. Artificial organs 40(10):971–980

Ding J, Chen Z, Niu S, Zhang J, Mondal NK, Griffith BP, Wu ZJ (2015) Quantification of shear-induced platelet activation: high shear stresses for short exposure time. Artificial organs 39(7):576–583

Dodsworth L (2016) Operational parametric study of a prototype tesla pump. Master's thesis, Dalhousie University

Dorman FD, Murphy TE, Blackshear PL (1966) An application of the tesla viscous flow turbine to pumping blood: Mechanical devices to assist the failing heart. national research council. In: National Academy of Science, pp 119–128

Farinas MI, Garon A, Lacasse D, N'dri D (2006) Asymptotically consistent numerical approximation of hemolysis. Journal of Biomechanical Engineering 128(5):688–696, DOI 10.1115/1.2241663, URL https://doi.org/10.1115/1.2241663, https://asmedigitalcollection.asme.org/biomechanical/article-pdf/128/5/688/5621900/688_1.pdf

Farrell PE, Ham DA, Funke SW, Rognes ME (2013) Automated derivation of the adjoint of high-level transient finite element programs. SIAM Journal on

Scientific Computing 35(4):C369–C393

Forchheimer P (1901) Wasserbewegung durch boden. Z Ver Deutsch, Ing 45:1782–1788

Fraser K, Taskin M, Zhang T, Griffith B, Wu Z (2010) Comparison of shear stress, residence time and lagrangian estimates of hemolysis in different ventricular assist devices. In: 26th Southern Biomedical Engineering Conference SBEC 2010, April 30-May 2, 2010, College Park, Maryland, USA, Springer, pp 548–551

Garon A, Farinas MI (2004) Fast three-dimensional numerical hemolysis approximation. Artificial Organs 28(11):1016–1025

Ghattas O, He B, Antaki JF, et al. (1995) Shape optimization of navier-stokes flows with application to optimal design of artificial heart components. Tech. rep., Carnegie Institute of Technology, Department of Civil and Environmental Engineering

Giersiepen M, Wurzinger L, Opitz R, Reul H (1990) Estimation of shear stress-related blood damage in heart valve prostheses-in vitro comparison of 25 aortic valves. The International journal of artificial organs 13(5):300–306

Gijsen FJH, van de Vosse FN, Janssen JD (1999) The influence of the non-newtonian properties of blood on the flow in large arteries: steady flow in a carotid bifurcation model. Journal of Biomechanics 32(6):601–608, DOI https://doi.org/10.1016/S0021-9290(99)00015-9, URL `http://www.sciencedirect.com/science/article/pii/S0021929099000159`

Grigioni M, Morbiducci U, D'Avenio G, Di Benedetto G, Del Gaudio C (2005) A novel formulation for blood trauma prediction by a modified power-law mathematical model. Biomechanics and Modeling in Mechanobiology 4(4):249–260

Gurtin ME (1981) An introduction to continuum mechanics, 1st edn. Academic Press, New York

Hansen KB, Arzani A, Shadden SC (2015) Mechanical platelet activation potential in abdominal aortic aneurysms. Journal of biomechanical engineering 137(4)

Hasinger SH, Kehrt LG (1963) Investigation of a shear-force pump. Journal of Engineering for Power 85(3):201–206

Hellums JD (1994) 1993 whitaker lecture: biorheology in thrombosis research. Annals of biomedical engineering 22(5):445–455

Hinghofer-Szalkay H, Greenleaf J (1987) Continuous monitoring of blood volume changes in humans. Journal of applied physiology 63(3):1003–1007

Hyun J, Wang S, Yang S (2014) Topology optimization of the shear thinning non-newtonian fluidic systems for minimizing wall shear stress. Computers & Mathematics with Applications 67(5):1154 – 1170, DOI https://doi.org/10.1016/j.camwa.2013.12.013, URL `http://www.sciencedirect.com/science/article/pii/S0898122113007074`

Izraelev V, Weiss WJ, Fritz B, Newswanger RK, Paterson EG, Snyder A, Medvitz RB, Cysyk J, Pae WE, Hicks D, et al. (2009) A passively-suspended tesla pump left ventricular assist device. ASAIO journal (American Society for Artificial Internal Organs: 1992) 55(6):556

Jensen KE (2013) Structural optimization of non-newtonian microfluidics. PhD thesis, Technical University of Denmark, phD thesis

Jiang L, Chen S, Sadasivan C, Jiao X (2017) Structural topology optimization for generative design of personalized aneurysm implants: Design, additive manufacturing, and experimental validation. In: 2017 IEEE Healthcare Innovations and Point of Care Technologies (HI-POCT), IEEE, pp 9–13

Kian JdM (2017) Topology optimization method applied to design channels considering non-newtonian fluid flow. Master's thesis, Universidade de São Paulo, URL `http://www.teses.usp.br/teses/disponiveis/3/3152/tde-16032017-103709/en.php`

Kini V, Bachmann C, Fontaine A, Deutsch S, Tarbell J (2001) Integrating particle image velocimetry and laser doppler velocimetry measurements of the regurgitant flow field past mechanical heart valves. Artificial organs 25(2):136–145

Lai WM, Rubin DH, Krempl E, Rubin D (2009) Introduction to continuum mechanics. Butterworth-Heinemann

Lazarov BS, Sigmund O (2010) Filters in topology optimization based on helmholtz-type differential equations. International Journal for Numerical Methods in Engineering 86(6):765–781

Leondes C (2000) Biomechanical Systems: Techniques and Applications, Volume II: Cardiovascular Techniques, 1st edn. Biomechanical Systems: Techniques and Applications, CRC Press

Logg A, Mardal KA, Wells G (2012) Automated solution of differential equations by the finite element method: The FEniCS book, vol 84. Springer Science & Business Media, URL `https://fenicsproject.org/book/`

Mitusch S, Funke S, Dokken J (2019) dolfin-adjoint 2018.1: automated adjoints for fenics and firedrake. Journal of Open Source Software 4(38):1292, URL `https://doi.org/10.21105/joss.01292`

Monroe DM, Hoffman M, Roberts HR (2002) Platelets and thrombin generation. Arteriosclerosis, thrombosis, and vascular biology 22(9):1381–1389

Montevecchi F, Inzoli F, Redaelli A, Mammana M (1995) Preliminary design and optimization of an ecc blood pump by means of a parametric approach. Artificial organs 19(7):685–690

Munson BR, Young DF, Okiishi TH (2009) Fundamentals of fluid mechanics, 6th edn. John Wiley & Sons, Inc.

Nam J, Behr M, Pasquali M (2011) Space-time least-squares finite element method for convection-reaction system with transformed variables. Computer methods in applied mechanics and engineering 200(33-36):2562–2576

Nobili M, Sheriff J, Morbiducci U, Redaelli A, Bluestein D (2008) Platelet activation due to hemodynamic shear stresses: damage accumulation model and comparison to in vitro measurements. ASAIO journal (American Society for Artificial Internal Organs: 1992) 54(1):64

Packham MA (1994) Role of platelets in thrombosis and hemostasis. Canadian journal of physiology and pharmacology 72(3):278–284

Pauli L, Nam J, Pasquali M, Behr M (2013) Transient stress-based and strain-based hemolysis estimation in a simplified blood pump. International journal for numerical methods in biomedical engineering 29(10):1148–1160

Philippi B, Jin Y (2015) Topology optimization of turbulent fluid flow with a sensitive porosity adjoint method (spam). arXiv:151208445

Pratumwal Y, Limtrakarn W, Muengtaweepongsa S, Phakdeesan P, Duangburong S, Eiamaram P, Intharakham K (2017) Whole blood viscosity modeling using power law, casson, and carreau yasuda models integrated with image scanning u-tube viscometer technique. Songklanakarin Journal of Science & Technology 39(5)

Reddy JN, Gartling DK (2010) The finite element method in heat transfer and fluid dynamics, 3rd edn. CRC press

Rey Ladino AF (2004) Numerical simulation of the flow field in a friction-type turbine (tesla turbine). Diploma thesis, Institute of Thermal Powerplants, Vienna University of Technology

Romero J, Silva E (2014) A topology optimization approach applied to laminar flow machine rotor design. Computer Methods in Applied Mechanics and Engineering 279(Supplement C):268 – 300, DOI https://doi.org/10.1016/j.cma.2014.06.029, URL `http://www.sciencedirect.com/science/article/pii/S0045782514002151`

Romero JS, Silva ECN (2017) Non-newtonian laminar flow machine rotor design by using topology optimization. Structural and Multidisciplinary Optimization 55(5):1711–1732

Sabersky RH, Acosta AJ, Hauptmann EG, Gates EM (1971) Fluid flow: a first course in fluid mechanics, vol 299. Macmillan

Sheriff J, Bluestein D, Girdhar G, Jesty J (2010) High-shear stress sensitizes platelets to subsequent low-shear conditions. Annals of biomedical engineering 38(4):1442–1450

Sheriff J, Soares JaS, Xenos M, Jesty J, Bluestein D (2013) Evaluation of shear-induced platelet activation models under constant and dynamic shear stress loading conditions relevant to devices. Annals of biomedical engineering 41(6):1279–1296

Soares JS, Sheriff J, Bluestein D (2013) A novel mathematical model of activation and sensitization of platelets subjected to dynamic stress histories. Biomechanics and modeling in mechanobiology 12(6):1127–1141

Sonntag RE, Borgnakke C (2013) Fundamentals of Thermodynamics, 8th edn. Wiley

Tesch K (2013) On invariants of fluid mechanics tensors. Task Quarterly 17(3-4):228–230

Travis BR, Marzec UM, Leo HL, Momin T, Sanders C, Hanson SR, Yoganathan AP (2001) Bileaflet aortic valve prosthesis pivot geometry influences platelet secretion and anionic phospholipid exposure. Annals of biomedical engineering 29(8):657–664

Wächter A, Biegler LT (2006) On the implementation of an interior-point filter line-search algorithm for large-scale nonlinear programming. Mathematical programming 106(1):25–57

Ward JC (1964) Turbulent flow in porous media. Journal of the Hydraulics Division 90(5):1–12

White FM (2009) Fluid Mechanics, 7th edn. McGraw-Hill, 2011

Wu J (2007) Letter to the editor: A possible major mistake in the paper entitled “collected nondimensional performance of rotary dynamic blood pump”: Smith wa, allaire p, antaki j, butler kc, kerkhoffs w, kink t, loree h, reul h. asaio journal 50: 25–32, 2004. Asaio Journal 53(2):255–256

Wu J, Antaki JF, Snyder TA, Wagner WR, Borovetz HS, Paden BE (2005) Design optimization of blood shearing instrument by computational fluid dynamics. Artificial organs 29(6):482–489

Yu H (2015) Flow design optimization of blood pumps considering hemolysis. PhD thesis, Magdeburg, Universität, Diss., 2015

Yun SH, Sim EH, Goh RY, Park JI, Han JY (2016) Platelet activation: the mechanisms and potential biomarkers. BioMed research international 2016

Zhang B, Liu X (2015) Topology optimization study of arterial bypass configurations using the level set method. Struct Multidiscip Optim 51(3):773–798, DOI 10.1007/s00158-014-1175-y, URL `http://dx.doi.org/10.1007/s00158-014-1175-y`

Zhang B, Liu X, Sun J (2016) Topology optimization design of non-newtonian roller-type viscous micropumps. Structural and Multidisciplinary Optimization 53(3):409–424

Appendix A Finite element formulation for the fluid flow problem

In order to define the finite element formulation, its is necessary to first define the corresponding boundary value problem. By considering the types of computational domains illustrated in Fig. 29, (Alonso et al., 2019)

$$
\begin{aligned}
\rho\nabla\boldsymbol{v}\bullet\boldsymbol{v} &= \nabla\bullet\boldsymbol{T}(\mu(\dot{\gamma}_{\mathrm{m}})) + \rho\boldsymbol{f} - 2\rho(\boldsymbol{\omega}\wedge\boldsymbol{v}) && \\
&\quad - \rho\boldsymbol{\omega}\wedge(\boldsymbol{\omega}\wedge\boldsymbol{r}) + \boldsymbol{f}_r(\alpha) && \text{in } \Omega \\
\nabla\bullet\boldsymbol{v} &= 0 && \text{in } \Omega \\
\boldsymbol{v} &= \boldsymbol{v}_{in} && \text{on } \Gamma_{\mathrm{in}} \\
\boldsymbol{v} &= \boldsymbol{0} && \text{on } \Gamma_{\mathrm{wall}} \\
\boldsymbol{T}(\mu(\dot{\gamma}_{\mathrm{m}}))\bullet\boldsymbol{n} &= \boldsymbol{0} && \text{on } \Gamma_{\mathrm{out}} \\
v_r = 0 \text{ and } \frac{\partial v_r}{\partial r} = \frac{\partial v_\theta}{\partial r} &= \frac{\partial v_z}{\partial r} = \frac{\partial p}{\partial r} = 0 && \text{on } \Gamma_{\mathrm{sym}}
\end{aligned}
\tag{52}
$$

Fig. 29 shows the interior of the computational domain (Ω), and the boundaries (Γ_{in}, Γ_{wall}, Γ_{out}, and Γ_{sym}). On the inlet boundary (Γ_{in}), the velocity profile is fixed, while, on the walls (Γ_{wall}), the no-slip condition is set. On the outlet boundary (Γ_{out}), the stress free Neumann boundary condition is set, while $\boldsymbol{n}$ is the unit vector that is normal to the boundaries – i.e., pointing outside the computational domain, and being given, in the 2D swirl flow model, as $\boldsymbol{n} = (n_r,\ 0,\ n_z)$, and, in the 2D model, as $\boldsymbol{n} = (n_x,\ n_y)$. On the symmetry axis ($\Gamma_{\mathrm{sym}}$, used in one of the 2D swirl flow cases in Fig. 29), there is a symmetry axis boundary condition: the derivatives in relation to the r coordinate are zero, and the radial velocity is also zero. The stress tensor ($\boldsymbol{T}$) is indicated as $\boldsymbol{T}(\mu(\dot{\gamma}_{\mathrm{m}}))$, when considering the fluid being modeled from the non-Newtonian fluid model, in eq. (6).

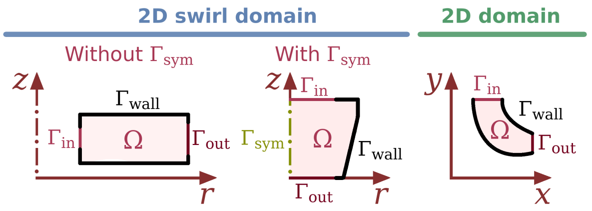

Fig. 29: Examples of boundaries for the fluid flow problems.

From the formulation presented in eq. (52), the finite element method is considered to solve the equilibrium equations for the 2D swirl flow model, by considering the weighted-residual and the Galerkin methods for the velocity-pressure (mixed) formulation, (Reddy and Gartling, 2010; Alonso and Silva, 2021)

$$R_c = \int_\Omega [\nabla \bullet \boldsymbol{v}] w_p r d\Omega \tag{53}$$

$$\begin{aligned} R_m = & \int_\Omega [\rho \nabla \boldsymbol{v} \bullet \boldsymbol{v} - \rho \boldsymbol{f} + 2\rho(\boldsymbol{\omega} \wedge \boldsymbol{v}) \\ & + \rho \boldsymbol{\omega} \wedge (\boldsymbol{\omega} \wedge \boldsymbol{r})] \bullet \boldsymbol{w}_v r d\Omega + \int_\Omega \boldsymbol{T}(\mu(\dot{\gamma}_{\mathrm{m}})) \bullet (\nabla \boldsymbol{w}_v) r d\Omega \\ & - \oint_\Gamma (\boldsymbol{T}(\mu(\dot{\gamma}_{\mathrm{m}})) \bullet \boldsymbol{w}_v) \bullet \boldsymbol{n} r d\Gamma + \int_\Omega \boldsymbol{f}_r(\alpha) \boldsymbol{v}_{\mathrm{mat}} \bullet \boldsymbol{w}_v r d\Omega \end{aligned} \tag{54}$$

where the equations are indicated by subscripts: c (denoting the *continuity equation*), and m (denoting the *linear momentum equation* – i.e., the Navier-Stokes equations). The corresponding test functions are indicated as: w_p (pressure test function), and $\boldsymbol{w}_v = \begin{bmatrix} w_{v,r} \\ w_{v,\theta} \\ w_{v,z} \end{bmatrix}$ (velocity test function). Since the integration domain ($2\pi r d\Omega$) includes a constant multiplier (2π), which exerts no influence when solving the weak form, eqs. (53) and (54) are given including a division by 2π (Alonso et al., 2019).

In the case of a 2D model, the integration domain is different (i.e., in Cartesian coordinates), meaning that, in eqs. (53) and (54), $rd\Omega$ should be replaced by $d\Omega$, while $rd\Gamma$ should be replaced by $d\Gamma$.

The test functions (w_p and $\boldsymbol{w}_v$) in eqs. (53) and (54) are mutually independent. This means that the corresponding equations may be summed, resulting in a single equation

$$F = R_c + R_m = 0 \tag{55}$$

Appendix B LSFEM formulation for the thrombosis model

The resulting LSFEM (Least Squares Finite Element Method) formulation from eqs. (27), (28), (29) and (30) becomes:

$$\int_\Omega \left[\frac{(\boldsymbol{v} \bullet \nabla) S_\tau}{\tau_{\mathrm{m}}} - 1 \right] [(\boldsymbol{v} \bullet \nabla) w_{S_\tau}] \, r d\Omega = 0 \tag{56}$$

$$\int_\Omega \left[\frac{(\boldsymbol{v} \bullet \nabla) D_{PAS,sl}}{\tau_{\mathrm{m}}^{\frac{\alpha_s}{\alpha_t}}} - 1 \right] [(\boldsymbol{v} \bullet \nabla) w_{D_{PAS,sl}}] \, r d\Omega = 0 \tag{57}$$

$$\int_\Omega \left[\frac{(\boldsymbol{v} \bullet \nabla) D_{PAS,sr}}{|(\boldsymbol{v} \bullet \nabla) \tau_{\mathrm{m}}|^{\frac{\delta_s}{\delta_t}}} - 1 \right] [(\boldsymbol{v} \bullet \nabla) w_{D_{PAS,sr}}] \, r d\Omega = 0 \tag{58}$$

$$\begin{aligned} & \Bigg\{ \frac{(\boldsymbol{v} \bullet \nabla) I_{PAS}}{S_\tau} - \Bigg[C_{PAS,S} I_{PAS} \\ & + \frac{C_{PAS,sl} \alpha_t D_{PAS,sl}^{\alpha_t - 1} (\boldsymbol{v} \bullet \nabla) D_{PAS,sl}}{S_\tau} \\ & + \frac{C_{PAS,sr} \delta_t D_{PAS,sr}^{\delta_t - 1} (\boldsymbol{v} \bullet \nabla) D_{PAS,sr}}{S_\tau} \Bigg] (1 - I_{PAS}) \\ & - \kappa_{PAS}(\alpha)(I_{PAS} - I_{PAS,\mathrm{mat}}) \Bigg\} \Big\{ (\boldsymbol{v} \bullet \nabla) w_{I_{PAS}} \\ & - \Big[C_{PAS,S} w_{I_{PAS}} S_\tau (1 - I_{PAS}) + \Big(C_{PAS,S} I_{PAS} S_\tau \\ & + C_{PAS,sl} \alpha_t D_{PAS,sl}^{\alpha_t - 1} (\boldsymbol{v} \bullet \nabla) D_{PAS,sl} \\ & + C_{PAS,sr} \delta_t D_{PAS,sr}^{\delta_t - 1} (\boldsymbol{v} \bullet \nabla) D_{PAS,sr} \Big) (-w_{I_{PAS}}) \Big] \\ & - \kappa_{PAS}(\alpha) w_{I_{PAS}} \Big\} \, r d\Omega = 0 \end{aligned} \tag{59}$$

where w_{S_τ}, $w_{D_{PAS,sl}}$, $w_{D_{PAS,sr}}$ and $w_{I_{PAS}}$ are the test functions.

Notice that $(\boldsymbol{v} \bullet \nabla) D_{PAS,sl}$ and $(\boldsymbol{v} \bullet \nabla) D_{PAS,sr}$ in eq. (30) can be substituted from eqs. (28) and (29), but the resulting system of equations would achieve a worse numerical conditioning (as has been observed in some tests). The numerical conditioning was observed to be much better when using the formulation presented in eq. (30).